2014

# Surface Effects on Critical Dimensions of Ferromagnetic Nanoparticles

Vartika Chaudhary
*Wright State University*

# SURFACE EFFECTS ON CRITICAL DIMENSIONS OF FERROMAGNETIC NANOPARTICLES

A thesis submitted in partial fulfillment of the
requirements for the degree of
Master of Science

By

Vartika Chaudhary
M.Sc. in Physics, Chaudhary Charan Singh University, 2009

2014
WRIGHT STATE UNIVERSITY

WRIGHT STATE UNIVERSITY

GRADUATE SCHOOL

August 7, 2014

I HEREBY RECOMMEND THAT THE THESIS PREPARED UNDER MY SUPERVISION BY Vartika Chaudhary ENTITLED Surface Effects on Critical Dimensions of Ferromagnetic Nanoparticles BE ACCEPTED IN PARTIAL FULFILLMENT OF THE REQUIREMENTS FOR THE DEGREE OF Master of Science.

_____

Gregory Kozlowski, Ph.D.
Thesis Director

_____

Doug Petkie, Ph.D.
Chair, Department of Physics

Committee on Final Examination

_____

Gregory Kozlowski, Ph.D.

_____

Doug Petkie, Ph.D.

_____

John Boeckl, Ph.D.

_____

Robert E. W. Fyffe, Ph.D.
Vice President for Research and
Dean of the Graduate School

## ABSTRACT

Chaudhary, Vartika. M.S. Department of Physics, Wright State University, 2014, Surface Effects on Critical Dimensions of Ferromagnetic Nanoparticles.

This work studies surface effects on the critical dimensions of ferromagnetic nanoparticles. Iron nanoparticles with different mean diameters from 5.9 nm to 21.4 nm used in this research were prepared by thermal decomposition of iron pentacarbonyl in the presence of oleic acid/octyl ether at Cambridge University, United Kingdom. Heating response of these ferromagnetic nanoparticles suspended in water were measured experimentally during which same amount of iron nanoparticles and di-ionized water were irradiated by an alternating magnetic field and the increase in temperature of these samples was measured. Heating performance of nanoparticles was described in terms of Specific Absorption Rate (SAR) which depends on the heating rate. Heating rate was calculated from the initial slope of heating curve at inflection point whereby there is minimum heat loss to the surrounding. Results were analyzed to find the critical diameters for the transition from single-domain to superparamagnetic regime and from single-domain to multi-domain regime. Also, frequency and current dependence of SAR was studied. The maximum value of SAR was obtained when applied frequency and current were at 175 kHz and 15 A, respectively. Equation for the critical radius for the transition from single-domain to multi-domain regime with low anisotropy was derived and numerically solved by using program written in C++ and results were analyzed to find the effect of surface parameters on the critical radius of nanoparticles.

The SAR vs nanoparticle's diameter shows two maxima which can be correlated to two critical dimensions. One is $D_{C1}$ at 18 nm for the transition from single-domain to multi-domain configuration and second is $D_{C2}$ at 10 nm for the transition from single-domain to superparamagnetic regime. Comparison of these experimental results with BOLS correlation theory has been done.

## TABLE OF CONTENTS

Page

## LIST OF FIGURES

Page

## LIST OF TABLES

Page

ACKNOWLEDGEMENTS

I would like to express my profound gratitude and deep regards to Dr. Gregory Kozlowski, my research supervisor, for his patient and excellent guidance, constructive and valuable suggestions, continuous support and enthusiastic encouragement. His willingness to give his precious time has been very much appreciated. The knowledge gained from him has been priceless and without his efforts and encouragement this Thesis would not have been completed. I will be greatly indebted and thankful to Dr. K throughout my life. My heartfelt Thanks to you, Dr. K.

I would like to take this opportunity to express a deep sense of gratitude to Dr. Doug Petkie, my Department Chair, for his support, valuable information and guidance, which helped me a lot in completing my degree. I also would like to thank him for agreeing to be on my Thesis committee.

I would like to give a special thanks to Dr. John Boeckl for his willingness to be on my Thesis committee.

I would also like to thank all my Professors, and staff members of the Physics Department of Wright State University for their kind co-operation and willingness to share knowledge with me.

I would like to give special thanks to Xing Zhao and Deema Aldaife, my friends, colleagues and lab-mates, for always being there for me. I find myself lucky to have friends like them in my life.

I would like to give my deepest gratitude and love to my parents, my sisters Geetika Singh and Shilpa Singh, my brother Akshit Chaudhary and my brother-in-law Lokendra

Singh for loving and supporting me every single day, for always standing by my side and lifting me up whenever I feel stuck in any situation, for telling me what I am capable of and for always believing in me. I would lovingly like to thank, my little nieces Yashna and Aadya, for their love. Thank you!

# DEDICATION

I lovingly dedicate this thesis to my parents Mr. Rishi pal Singh and Mrs. Mithlesh Singh, who have given me so much love and blessings. They have shown so much faith in me, and given me the liberty to choose what I desire. There are not enough words in the world to express my gratitude to them, but without each of them, I would not be the person I am still and still working on becoming.

# I. INTRODUCTION

A nanoobject is a physical object differing in properties from the corresponding bulk material and having at least one dimension between 1 nm and 100 nm. The magnetic properties of nanoparticles are determined by various factors like shape and size of particle, chemical composition, type and degree of defectiveness of crystal lattice, strong interactions of nanoparticles with neighboring nanoparticles as well as surrounding matrix, higher number of surface atoms as comparison to core, very large amount of low-coordinated atoms at edges and corner sites, and the enhanced importance of thermal fluctuations on the dynamical behavior [1]. For example, the contribution of the surface atoms to the physical properties increases with decreasing nanoparticle sizes. Since the area of the surface of nanoparticles varies with square of its radius ~ $R^2$, while the volume of the samples varies as ~ $R^3$. The fraction of atoms at the surface with respect to the volume of the nanoparticle, varies with surface area divided by volume. As a consequence, the ratio of surface to volume varies roughly as inverse of radius $R^{-1}$. Thus, number of atoms on the surface increases with decreasing particle size. Surface atoms have fewer number of neighboring atoms as comparison to the bulk due to which nanoparticles with large fraction of atoms on the surface have a low coordination number (number of nearest neighbors) [1]. Tuning these properties of magnetic nanoparticles can allow us to tailor nanoparticles for specific applications, thus increasing their effectiveness. For instance, in biosensing, cubic nanoparticles with higher saturation magnetization Ms are preferred because of their higher sensitivity, efficiency and increase in contact area of a cube (that reflects effect of geometry on nanoparticles). And it was also studied that saturation magnetization increases linearly with size until it reaches the bulk value [2]. Due to unique size and different physical, chemical, thermal and mechanical properties magnetic

nanoparticles are widely used as agents for drug delivery to target tissues, tissue repair, cell labelling, magnetic resonance imaging, and tumor hyperthermia [2]. Moreover, magnetic nanomaterials have a great advantage in providing selective attachment and giving magnetic properties to a target, by a special surface coating (non-toxic and biocompatible) which allows the use of nanoparticles as targetable delivery with nanoparticle localization in specific area. By controlling magnetic field, manipulation and transportation of the magnetic nanoparticles can be realized [3]. These magnetic nanoparticles can bind to proteins, enzymes, drugs, antibodies, etc., and can be directed to an organ, tissue or tumor with the help of an external or alternating magnetic field for use in hyperthermia [2].

Due to the use of magnetic materials in wide range of disciplines like magnetic fluids, catalysis, biotechnology, data storage and environmental remediation some special methods for the synthesis of magnetic nanoparticles of various different compositions and their successful use in these areas are really important, which depends on the stability of the nanoparticle under the range of different conditions. For instance, in many applications iron oxide nanoparticles in single-domain range with typical size of 10 nm − 20 nm perform really well because these nanoparticles show superparamagnetic behavior when the temperature is above the blocking temperature. These nanoparticles with large magnetic moment behave like giant paramagnetic atoms and show very fast response to applied magnetic field with negligible remanence (residual magnetism) and coercivity (the magnetic field required to bring the magnetization to zero). So, these superparamagnetic nanoparticles are very useful in broad range of biomedical applications as they have negligible risk of forming agglomeration at room temperature [4].

**GOALS OF MY THESIS**

Goals of my research are to have theoretical and experimental understanding of surface effects

on the critical size of ferromagnetic (iron) nanoparticles and how magnetic properties of nanoparticles depend on size. Doing that we get insight into the critical size of nanoparticles for single-domain, multi-domain and superparamagnetic regime and derive equation for a critical size of nanoparticles for single-domain to multi-domain transition at low to high anisotropy. Iron nanoparticles used here were prepared by thermal decomposition of iron precursor method in Cambridge University, United Kingdom. During this method, iron pentacarbonyl [$Fe(CO)_5$] was decomposed at high temperature to get iron nanoparticles of mean diameter between 5.9 nm to 21.4 nm. Initially, different sets of heating measurements with iron nanoparticles, placed in ac magnetic field are performed to determine the critical sizes with the help of specific absorption rate (SAR) plots which will also show the heating efficiency of a nanoparticle and effects of frequency, current and particle size on heating performance. The effect of surface layer on magnetic properties and critical size of nanoparticles is achieved by solving numerically the equation for the critical size of iron nanoparticle for transition from single-domain to multi-domain regime by program written in C++. A clear understanding of surface effects on critical size can be achieved by finding dependence between critical radius and surface parameters such as surface magnetization, anisotropy or exchange interaction. The reasoning behind the discrepancy between experimentally found critical sizes in iron nanoparticles could be based and successfully explained in terms of surface effects.

**CHAPTERS SUMMARY**

Chapter I (Introduction) outlines on the importance and uses of magnetic nanoparticles. In this chapter, goals of my research are clearly stated with Thesis outline underlined.

Chapter II (Magnetism) reviews fundamental concept of magnetism with concentration on different type of magnetic materials and their responses to applied magnetic field. Following that,

nanomagnetism will be explained with the detailed concept of a new phase called superparamagnetism.

Chapter III (Magnetic Domains) elaborates on the process of formation of magnetic domains and on the process of magnetization including hysteresis loop. The critical sizes will be presented involving transition from single-domain to superparamagnetic phase of ferromagnetic nanoparticles or to multi-domain structure. Further, this chapter will deal with different anisotropy energies.

Chapter IV (Critical Size of Ferromagnetic Nanoparticles) outlines derivation of the equation for the critical radius of ferromagnetic nanoparticles for transition from single-domain to multi-domain configuration with low and high anisotropy. This will be achieved by comparing the energies of both configurations.

Chapter V (Surface Effects) deals with effect of nanoparticle surface on its critical size and explains how magnetic properties such as saturation magnetization, anisotropy, Curie temperature and exchange integral change when the bulk size material reduces to nanometer scale. In this chapter, the equation describing critical size of ferromagnetic nanoparticle for the transition from single-domain to multi-domain configuration will be rewritten in terms of surface parameters including their effect on the critical size.

Chapter VI (Heat Mechanisms in Ferromagnetic Nanoparticles) elaborates on the different type of heating mechanisms for magnetic nanoparticles due to applied ac magnetic field. The heating associated with hysteretic losses in ferromagnetism will be addressed which can be quantified by area enclosed by hysteresis curve. The relevant equations for the power will be derived. The heating associated with superparamagnetic nanoparticles based on Neel and Brown relaxation mechanisms will also be addressed.

Chapter VII (Synthesis and Characterization of Ferromagnetic Nanoparticles) details the synthesis and some properties of iron nanoparticles used for this research.

Chapter VIII (Experimental Setup for Measurement of Heating Rate and Specific Power Loss) outlines experimental setting and procedures used for the heating of magnetic nanoparticles in the presence of externally applied alternating magnetic field.

Chapter IX (Experimental Results) summarizes the results from heating experiments carried out on iron nanoparticles dispersed in de-ionized water. Heating rate of iron nanoparticles are calculated from the initial slope of temperature vs time and heating performance of magnetic nanoparticles will be described in terms of Specific Power Loss (SPL) or Specific Absorption Rate (SAR). A relevant equation for SAR will be derived.

Chapter X (Discussion) analyses the results from all the performed experiments and conclusions will be drawn from analysis of the experimental data. Effect of average nanoparticle radius on SAR resulted in establishing critical size for the single-domain to superparamagnetic and to multi-domain transition, respectively. Dependence of applied frequency and current on SAR will also be discussed. In this chapter, a program written in C++ to solve the critical size equation for the transition from single-domain to multi-domain configuration of iron nanoparticle are shown and an analysis will be done on the effect of surface parameters on the critical radius of iron nanoparticles. At the same time, critical sizes of iron nanoparticles from my measurements are established and compared with other existing measurements in literature.

Chapter XI (Conclusion and Future Goals) concludes Thesis by summarizing the important results and suggests ideas for future research.

## II. MAGNETISM

Scottish physicist and mathematician James Clark Maxwell derived fundamental equations known as Maxwell's equations which laid the foundation of electromagnetism. They describe how electric and magnetic field are generated and altered by each other as well by charges and currents. In differential form, Maxwell's equations are given as follows:

$$\boldsymbol{\nabla} \cdot \boldsymbol{E} = \frac{\rho}{\epsilon_0} \tag{1}$$

$$\boldsymbol{\nabla} \cdot \boldsymbol{B} = 0 \tag{2}$$

$$\boldsymbol{\nabla} \times \boldsymbol{E} = -\frac{\partial \boldsymbol{B}}{\partial t} \tag{3}$$

$$\boldsymbol{\nabla} \times \boldsymbol{B} = \mu_0 \boldsymbol{J} + \mu_0 \varepsilon_0 \frac{\partial \boldsymbol{E}}{\partial t} \tag{4}$$

Eq. (1) is known as Gauss's law showing how electric field $\boldsymbol{E}$ is formed by a charge density $\rho$ and $\varepsilon_0$ is the permittivity of free space. Eq. (2) is famous Gauss's law for magnetism, where $\boldsymbol{B}$ is a magnetic field. There is a break of symmetry in this equation as compared to Eq. (1) as there are no magnetic monopoles in contrast to electric single charges. Eq. (2) assumes that the simplest magnetic structure that can exist is a magnetic dipole and magnetic monopoles do not exist. Nevertheless, it was pointed out by Pierre Curie [5], [6] that magnetic monopoles could conceivably exist, despite not having been seen so far. Later Paul Dirac showed that if any magnetic monopoles exist in the universe, then all electric charges in the universe must be quantized. The electric charge is quantized but does not prove the existence of monopole [6], [7]. However, a group from the University of Cologne [7] has produced artificial magnetic monopoles in 2013 resembling those postulated in 1931 by Paul Dirac. Eq. (2) also postulated that magnetic field lines always form continuous loops. Which implies zero magnetic flux on the right hand side of the Eq. (2) as all closed surfaces have the same number of magnetic field lines going in as coming out. Magnetic dipoles which are basically current loops produce the required magnetic

fields. Eq. (3) is known as Faraday's law of induction and represents how a time varying magnetic field produces an electric field. Finally, Eq. (4) is the Ampere's circuit law describing how an electric current density $\boldsymbol{J}$ and a time varying electric field $\boldsymbol{E}$ produce a magnetic field. In this equation constant $\mu_0$ is the magnetic permeability of free space.

The magnetization $\boldsymbol{M}$ is the vector field describing the density of permanent or induced magnetic dipole moments in magnetic material [4]. It is the measure of strength of magnetism in a material and depends on the density of magnetic moments n and their magnitudes $\mu_s$ (see Eq. (5)),

$$M = (N/V)\mu_s = n\mu_s \tag{5}$$

where N is the number of magnetic moments in a volume. Net magnetization results from interaction of magnetic moments with an externally applied magnetic field and also interaction with neighboring magnetic moments (i.e., ferromagnetic materials). The origin of the magnetic moments creating magnetization of the material can be either due to the orbital motion of the electron or due to spin of the electron [8]. The relation between net magnetization and applied magnetic field [5] is given by Eq. (6),

$$\boldsymbol{M} = \chi \boldsymbol{H} \tag{6}$$

where $\chi$ is the magnetic susceptibility of the material. The relation [9] between permeability of the material μ, the permeability of free space $\mu_0$, and the magnetic susceptibility $\chi$ is given by Eq. (7)

$$\chi = \frac{\mu}{\mu_0} - 1 \tag{7}$$

The response of a material to an external magnetic field is called magnetic induction $\boldsymbol{B}$. The relation between magnetic induction and net magnetizing field [9] is given by Eq. (8),

$$\boldsymbol{B} = \mu_0(\boldsymbol{H} + \boldsymbol{M}) = \mu_0(1 + \chi)\boldsymbol{H} = \mu_0\mu_r\boldsymbol{H} \tag{8}$$

where $\mu_r = \frac{\mu}{\mu_0} = 1 + \chi$ is the relative permeability (for vacuum $\mu_r = 1$, for matter $\mu_r \geq 1$ generally and possible to have a value of around 100,000).

**TYPES OF MAGNETIC MATERIALS**

Magnetic behavior of magnetic materials is governed by the interaction of magnetic dipole moments of its atoms with an externally applied magnetic field. Based on the response of magnetic materials to an applied magnetic field, we can divide magnetic materials into three main categories (diamagnetic, paramagnetic, and ferromagnetic) as described below.

**DIAMAGNETIC MATERIALS**

Diamagnetic material possesses no magnetic moment in atoms, ions or molecule which they constitute. In the presence of an externally applied magnetic field, there is a creation of circulating atomic currents that produce a very small magnetic moment per unit volume which opposes the applied field. This can be explained in terms of Lenz's law, according to which when a magnetic field is applied to a circuit, a current is induced in order to reduce the increased magnetic flux caused by magnetic field which means that the circuit has a magnetic moment opposite to the externally applied magnetic field [10]. The magnetic susceptibility of diamagnetic material, which is the measure of the extent to which a magnetic material may be magnetized in relation to the externally applied magnetic field (see, Eq. (9), [11]),

$$\chi = -\frac{N}{V}\frac{\mu_0 e^2}{6m}\sum_i \langle r_i{}^2 \rangle \tag{9}$$

In diamagnetic materials only outermost shells significantly contribute to $\chi$ which is proportional to $\langle r_i{}^2 \rangle$ (average of squared radius of electron orbit $r_i$). This situation is characterized by no unpaired electrons which imply a vanishing magnetic moment without an external magnetic field. The temperature dependence of susceptibility of diamagnetic substance is negligible (see, Fig. 1).

## PARAMAGNETIC MATERIALS

Paramagnetic material have a net angular momentum due to unpaired electrons. This is a non-vanishing magnetic moment. In the absence of externally applied magnetic field no favored orientation of the magnetic moments occurs and resulting magnetization tends to zero. But in the presence of externally applied magnetic field these magnetic moments orient themselves in the direction of applied field and give rise to induced magnetization. The total magnetization depends on the magnitude of externally applied magnetic field B and temperature T (see, Eq. (10)),

$$M \propto B/T \tag{10}$$

The magnetism of paramagnetic materials mostly originates from the presence of permanent magnetic moment with negligible interaction with each other. These moments can orient themselves freely in any direction creating so called paramagnetism of free atoms. Fig. 1 is showing magnetization *M* vs applied field *H* and Curie law for paramagnetic susceptibility.

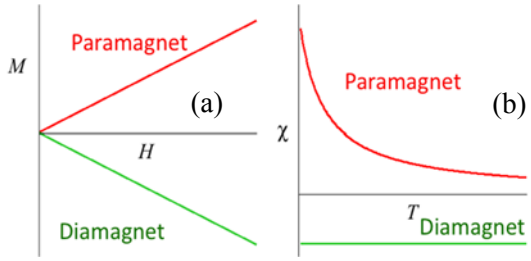


Fig. 1. Magnetization vs applied field (a) and susceptibility vs temperature (b) for paramagnetic and diamagnetic materials.

Paramagnetic materials have low positive susceptibility, i.e., the magnetization *M* is oriented parallel to an external magnetic field *H*. This susceptibility is dependent of the temperature and defined as follows

$$\chi = n\frac{\mu_0}{3k_BT}{\mu_{eff}}^2 \tag{11}$$

where $\mu_{eff} = g_J \mu_B \sqrt{J(J+1)}$ is the effective magnetic moment, n is the number of magnetic moments per unit volume, $g_J$ is the Lande factor, $J$ is the total angular momentum, $k_B$ is the Boltzmann constant, $T$ is temperature, and $\mu_B$ is the Bohr magneton. Above Eq. (11) can be written as Curie law (see, Eq. (12)),

$$\chi = \frac{C_{Curie}}{T} \tag{12}$$

where $C_{Curie} = n \frac{\mu_0}{3k_B} {\mu_{eff}}^2$. For high magnetic fields, $J(J+1) \sim J^2$ and the effective magnetic moment is now $\mu_{eff} = g_J \mu_B J$ [11].

The induced magnetization is lower when temperature is higher due to thermal agitation. The low field susceptibility is positive, becomes infinity at zero Kelvin, and decreases when temperature is increased due to randomizing effect of thermal excitations. This susceptibility is of the order of $10^{-3}$ – $10^{-5}$ at room temperature.

**FERROMAGNETIC MATERIALS**

Ferromagnets exhibit magnetic moments which are aligned parallel to each other. Ferromagnetism is characterized by spontaneous magnetization Ms in the absence of an external magnetic field due to the alignment of all magnetic moments in microscopically large region called a domain parallel to each other in same direction. When magnetic field is applied, domain enlarges in size and causes moments in different domains to align in the direction of magnetic field and there is a huge net magnetic moment or saturation magnetization (see, Fig. 2). Upon removal of the field, a considerable amount of the moments are still left aligned, giving a remanence magnetization. In other words, when external field is applied to a ferromagnetic material and removed, the magnetization does not follow the initial magnetization curve called virgin curve but this gives rise to hysteresis loop.

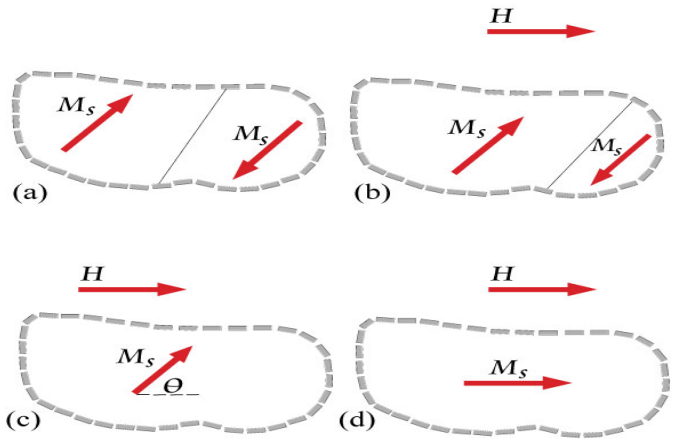


Fig. 2. Process of magnetization in a demagnetized ferromagnetic material [12].

Although the material is ferromagnetic, it consists of a number of ordered domains arranged randomly giving no net magnetization. As can be seen from Fig. 2, with two domains whose individual saturation magnetizations $M_s$ lie antiparallel to each other (Fig. 2a). As the magnetic field $H$ is applied those domains which are more energetically favorable with respect to the field, increase in size at the expense of those whose moment lie more antiparallel to $H$. There is now a net magnetization $M$ (Fig. 2b). Finally, with very strong field, all of the materials become single domain with all moments aligned parallel, or close to parallel, with $H$. The magnetization is now $M = M_s\cos\theta$ where $\theta$ is the angle between $M_s$ along the easy direction of magnetization and $H$ (Fig. 2c). Finally $M_s$ is rotated parallel to $H$ and the ferromagnet is saturated with a magnetization $M = M_s$ (Fig. 2d).

Ferromagnetism is the basic mechanism by which certain materials form permanent magnets. Permanent magnets are materials that can be magnetized by an external magnetic field and remain magnetized after the magnetic field is removed. These materials are either ferromagnetic or ferrimagnetic. Ferromagnetism is the strongest type of magnetism among all the magnetism mechanism like diamagnetism and paramagnetism. To gain more insight on ferromagnetic

materials, we have to understand exchange interactions which is entirely a quantum mechanical phenomenon existing between neighboring magnetic moments [11],[13].

We can differentiate different type of magnetic materials according to their behaviors at different temperature ranges. At zero temperature all moments are aligned parallel to each other in ferromagnetic materials. The ferromagnetism appears below a critical temperature $T_c$, called the Curie temperature, which depends on the material. Above this temperature materials are paramagnetic since the magnetic moments have random orientation. At absolute zero temperature, all the magnetic moments of a ferromagnetic material are frozen in a specific direction called crystallographic axis, such that the magnetization is saturated and as the temperature is increased, the overall magnetization decreases until it reaches a zero at Curie temperature $T_c$. Above $T_c$, the magnetization increases linearly (see, Fig. 3).

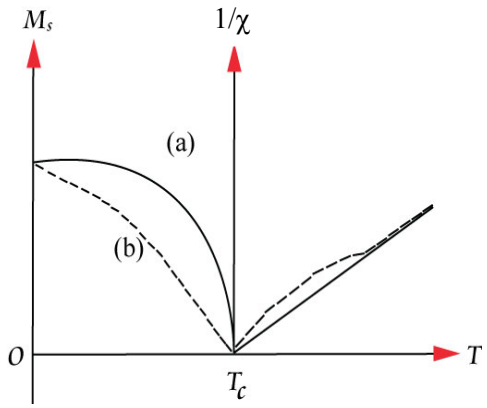


Fig. 3. Magnetization vs temperature for ferromagnetic (a) and ferrimagnetic (b) material [12].

**ANTIFERROMAGNETIC MATERIALS**

Perfect antiferromagnetic materials consist of two interpenetrating magnetic moments aligned in opposite directions with resultant magnetization equals zero. Above critical temperature called Neel temperature $T_N$ [14], antiferromagnetic materials behave as paramagnetic materials. Antiferromagnetism has a weak form of magnetism with weak and positive susceptibility. The

reciprocal susceptibility is varying linearly with the temperature and follows the Curie law (see, Fig. 4) above $T_N$. The maximum in susceptibility comes from the appearance of an antiparallel arrangement of the magnetic moments. Thermal variation of reciprocal susceptibility exhibits a minimum at Neel temperature $T_N$. The susceptibility decreases as thermal agitation decreases when temperature is reduced below $T_N$. At high temperature, thermal agitation overcomes interaction effects and thermal variation of the susceptibility is similar to paramagnetic materials. Thus, above the Neel temperature the materials are typically paramagnetic. In a magnetic field an antiferromagnetic material may display a ferromagnetic behavior [14].

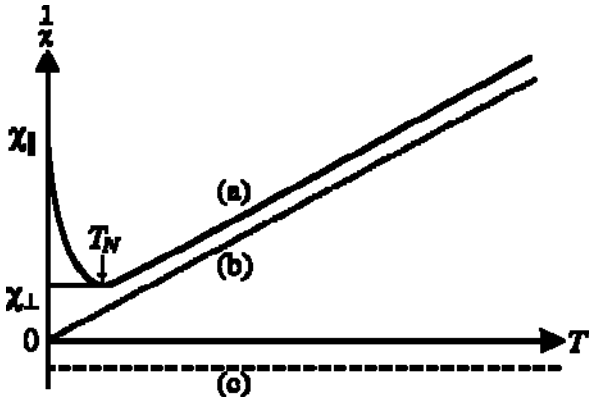


Fig. 4. Variation of reciprocal susceptibility with temperature for antiferromagnetic (a), paramagnetic (b), and diamagnetic ordering (c) [12].

## FERRIMAGNETIC MATERIALS

Ferrimagnetic materials has antiparallel orientation of magnetic moments as in antiferromagnetic materials, but they are not equal in magnitude so they do not balance each other completely, and hold spontaneous magnetization below the Curie temperature, [15]. Sometimes there is also another temperature below the Curie temperature, called the Neel temperature, at which the two opposing moments are equal, resulting in net zero magnetization. This is called magnetization compensation point and the material is then antiferromagnetic.

## NANOMAGNETISM

Nanomagnetism is the magnetism observed in magnetic nanoparticles. Nanomaterials due to their small sizes exhibit different magnetic behaviors and properties than bulk materials. Magnetization per atom, coercivity, magnetic anisotropy of a nanoparticle can be much greater than those of bulk materials while Neel or Curie temperature of nanoparticle and bulk material can have a difference of hundreds of degrees. Two finite-size effects occur in magnetic nanoparticles. One is superparamagnetic limit and another one is single-domain limit.

## SUPERPARAMAGNETISM

Magnetic nanoparticles exhibit a unique behavior in which thermal motion causes the magnetic moments to randomly flip directions, eliminating any remnant magnetization in the absence of an applied field. This behavior is known as superparamagnetism. This is due to the fact that below certain critical size, the anisotropy barrier $KV$ ($K$ is anisotropy of the material and $V$ is magnetic volume) of a magnetic crystal is reduced to the point where it can be overcome by the energy of thermal vibrations $k_BT$ ($k_B$ is the Boltzmann constant and $T$ is absolute temperature). Thus, below certain critical dimensions, magnetic nanoparticles exhibit magnetic responses reminiscent of those of paramagnetic materials, which is a zero average magnetic moment in the absence of an externally applied field and a rapidly increasing magnetic moment under the application of an externally applied field (in the direction of field). This phenomenon is observed at temperatures above the so-called blocking temperature $T_B$. The value of blocking temperature, associated with the energy barrier depends on the characteristics measurement time ($\tau_m$). Measurement time can vary from $100\ s$ to $10^{-8}\ s$ [16]. Remnant magnetization and hysteresis loss are not present in superparamagnetic regime but significant losses still occur due to moment relaxation mechanics.

Critical size $R_C$ for superparamagnetic behavior can be determined by assuming a spherical geometry and modifying the equation for probability of thermal relaxation [13] (Eqs. (13),(14))

$$\tau_m = \tau_0 \exp\left(\frac{KV}{k_B T}\right) \tag{13}$$

$$R_C = \sqrt[3]{\left[\frac{3}{4\pi} ln\left(\frac{\tau_m}{\tau_0}\right)\frac{k_B T}{K}\right]} \tag{14}$$

where $\tau_0$ is the attempt time $\approx 10^{-9}$ *s*, $k_B$ is Boltzmann's constant, $T$ is the absolute temperature, $V$ is the volume of magnetic material, and $K$ is the anisotropy constant. For small magnetic nanoparticles at high temperatures, the anisotropy energy becomes smaller than the thermal energy and the magnetization of single-domain particles will then fluctuate with a characteristic relaxation time given by the Neel-Brown expression given by Eq. (15)

$$\tau = \tau_0 \exp\left(\frac{KV}{k_B T}\right) \tag{15}$$

Experimentally, we are dealing with a measurement time $\tau_m$ which represents the time for which measurement is taken and magnetic behaviour arises from the relative difference between the measuring time and relaxation time. Depending on the value of relaxation time τ, we have two possibilities. Firstly, if the relaxation time τ is larger than the measurement time $\tau_m$, the system appears to be stuck and at given magnetic field we will have a fixed magnetization in a given direction, i.e., blocked (ferromagnetic) regime. Secondly, if the measurement time is greater than the relaxation time, the magnetization appears to fluctuate, i.e., superparamagnetic regime. As a result of it, the magnetization in average appears to be zero in time. The value of blocking temperature can be given by Eq. (16)

$$T_B = \frac{KV}{k_B \ln(\frac{\tau_m}{\tau_0})} \tag{16}$$

Where $V = 4\pi R^3/3$ is the volume of magnetic nanoparticle. We can see from Eq. (16), that blocking temperature increases with the size of nanoparticle. However, this equation is not necessarily valid

for larger nanoparticles [16]. Experimentally, the value of blocking temperature can be established by dc magnetometry measurements, in which, the merging point of the zero-field cooled (ZFC) and field-cooled (FC) magnetization curves takes place [4], [16]. In this process, sample is first cooled from room temperature in zero magnetic field (ZFC) and then is warmed up in magnetic field (FC). This time a small external field is applied and the temperature is gradually increased while measuring the magnetization of sample as a function of temperature. As temperature increases the system is disturbed by thermal energy and more moments acquire the energy to be aligned with the external field direction. The number of unblocked, aligned moments reaches a maximum value when blocking temperature is reached. Above the blocking temperature, the thermal energy is strong enough to randomize to magnetic moments which leads to decrease in magnetization. Fig. 5 shows the point where two curves merge at irreversibility temperature and reached maximum at blocking temperature $T_B$ on the ZFC curve.

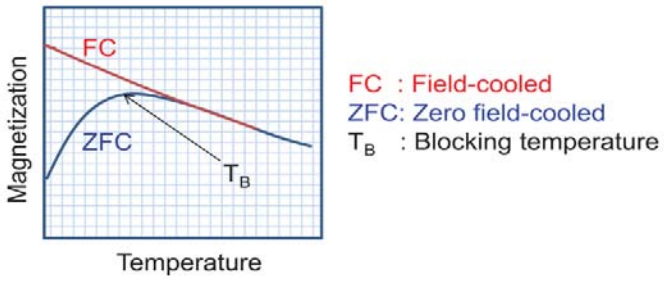


Fig. 5. ZFC/FC curve at different temperature [17].

Blocking temperature also depends on the anisotropy constant, the applied magnetic field and experimental measuring time. For instance, in ferromagnetic resonance technique, measurement of blocking temperature is done with a shorter time window $\tau \approx 10^{-9}\ s$, a larger value of blocking temperature is obtained as comparison to the values obtained from dc magnetization measurements. Moreover, a factor of two in particle diameter can change the reversal time from 100 years (the case of stable magnetism) to 100 nanoseconds (the case of superparamagnetism

with no remanence) [4]. Blocking temperature is very important parameter in the study of materials with nanometric size. We will discuss later that for the bulk material below Curie temperature, hysteresis effect is responsible for heat generation. However, for nanoscale materials, the material will lose its magnetization at the blocking temperature, and therefore will not produce heat below this temperature due to hysteretic effect and there will be relaxation losses responsible for heat then. A typical hysteresis curves for ferromagnetic, paramagnetic, diamagnetic, and superparamagnetic materials are shown in Fig. 6, as a contrast of their individual hysteresis behaviour. In the figure, as contrast to the hysteresis observed in the case of ferromagnetic material (red loop), the response of superparamagnetic nanoparticles to an external magnetic field also follows a sigmoidal curve but shows no hysteresis (green loop).

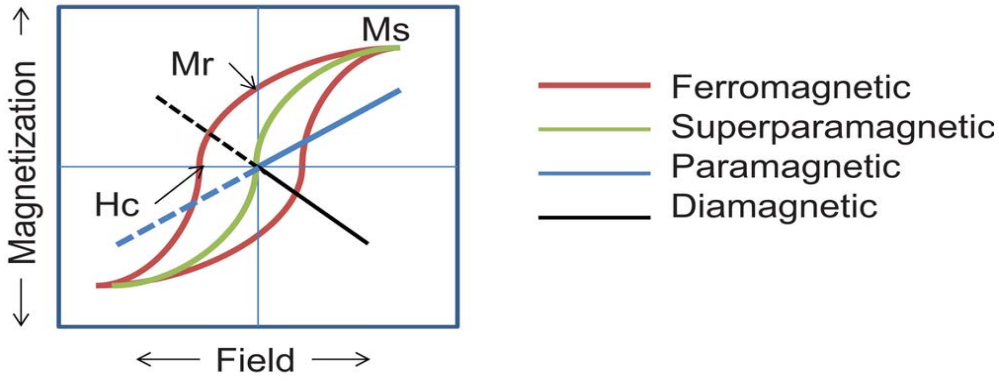


Fig. 6. Magnetic behavior of ferromagnetic, diamagnetic, paramagnetic, and superparamagnetic materials under the influence of an applied field showing saturation magnetization $M_S$, remanent magnetization $M_R$ and coercivity $H_c$ (the intensity of an external field needed to force the magnetization to zero) [16].

## III. MAGNETIC DOMAINS

Domain is a region of a magnetic material within which the local magnetization is saturated. Inside a particular domain, the individual magnetic moments of the atoms of a magnetic material are parallel to each other and align in the certain direction. However, the magnetization (magnetic moments per unit volume) of domains may point out in different directions.

### STUDY OF MAGNETIC DOMAINS: WEISS MOLECULAR FIELD

Before going into depth of a domain structure, we must discuss Weiss theory which plays a fundamental role in understanding of domain structure. The domain theory was first developed by French physicist Pierre-Ernest Weiss in 1906. He suggested that when a ferromagnetic material is cooled below the Curie temperature, its magnetization spontaneously divides into small regions of uniform magnetization. The direction of alignment of magnetic moments varies between domains but each domain is magnetized along easy magnetization axes. Weiss postulated the existence of a very strong internal magnetic field due to the long range order interactions between moments called Weiss molecular field. This field is responsible for the spontaneous alignment of magnetic moments in a ferromagnetic material [18]. The magnetization of a suitably prepared magnetic material can be changed from an initial value of zero (in absence of magnetic field) to a saturation value of the order of 1000 G, by the application of a very week magnetic field of the order of 0.01 Oe. This is not same in the case of a paramagnetic material in which the application of the field of 0.01 Oe can only increase the magnetization by $10^{-6}$ G. This is due to thermal agitations of magnetic moments which act to oppose the ordering influenced by applied magnetic field. The direction of the magnetic moments of a paramagnetic material remains random in the absence of external magnetic field. The existence of a powerful internal magnetic field in a ferromagnetic material circumvented the thermal agitations and as a result all the magnetic moments of a

ferromagnetic material orient parallel to each other leading to spontaneous magnetization. At Curie temperature, the thermal energy is sufficient to overcome the energy of interaction between the magnetic moments. This temperature at which the ferromagnetic behavior disappears is called Curie temperature.

Curie temperature $T_c$ is defined as follows (Eq. (17)),

$$\mu_B H_{mf} = k_B T_c \qquad (17)$$

where $k_B = 1.38 \times 10^{-23}$ J/K is the Boltzmann constant, $\mu_B = 0.927 \times 10^{-24}$ J/T is Bohr's magneton and $H_{mf}$ is the Weiss molecular field. Replacing $T_c = 1043$ K in Eq. (17) for Fe we can estimate a strength of molecular field $H_{mf} = 155$ T in this magnetic material. Below Curie temperature magnetic material behaves as a ferromagnet (Fig. 7a) but above $T_c$ magnetic disorder (Fig. 7b) is established which characterizes a paramagnetic phase. This magnetic disorder changes to parallel array of magnetic moments in the presence of externally applied magnetic field (Fig. 7c).

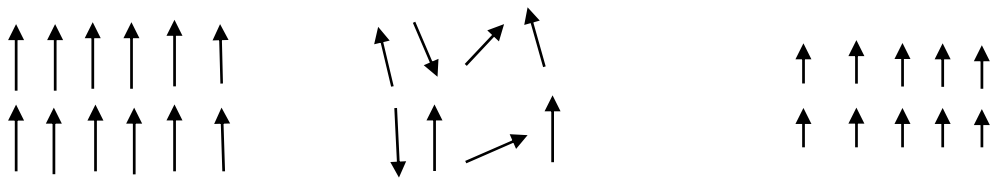


Fig. 7. Magnetic moment arrays in ferromagnetic (a) and paramagnetic (b) phase below and above Curie temperature. Paramagnet in presence of applied magnetic field (c).

**SINGLE-DOMAIN TO MULTI-DOMAIN CRITICAL SIZE**

So far we have discussed the factors that lead to the formation of ferromagnetic materials. Further, we will see why domain structure is formed in these materials. The simple answer is to minimize its total magnetic energy of the material. But before going further, we will have little insight on

the concept of critical size. Critical size corresponds to a transition from the single-domain to superparamagnetic and single-domain to multi-domain regime. If the size of magnetic nanoparticles is maintained below a critical dimension during nanoparticle synthesis, they tends to develop as single magnetic domain structure, and at the smallest sizes, they exhibit superparamagnetic behavior under some standard conditions as described in previous chapter on magnetism. The single-domain to multi-domain critical size corresponds to the point where it is energetically favorable for the magnetic nanoparticle to exist without a single domain wall [16]. In large magnetic nanoparticles, it is obvious that there should be multi-domain structure to minimize overall energy of the system.

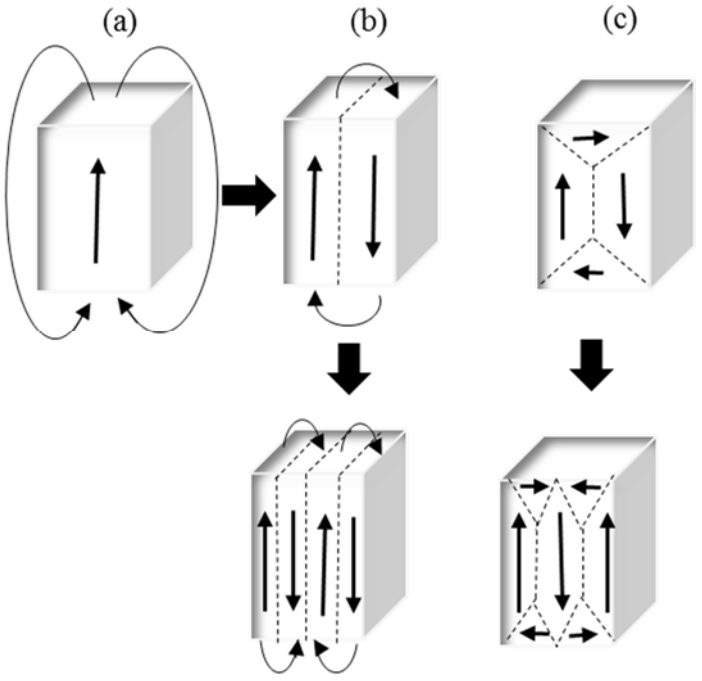


Fig. 8. Single-domain (a), multi-domain (b), and magnetic flux closure structure (c).

Ferromagnetic material with a large saturation magnetization in certain direction throughout volume of the material leads to formation of large magnetic poles on the surface (Fig. 8a). It requires a lot of magnetostatic energy. This is the self-energy due to the interaction of the magnetic field created by the magnetization of the material in some part of the material on the neighbors.

To minimize this energy, ferromagnetic material splits into two different regions (domains) (Fig. 8b) with the magnetization in opposite directions in each domain. The energetically driven subdivision results in creation of the boundary layer separating two domains. These narrow zones of transition are known as domain wall or Bloch wall where the magnetization gradually changes direction over roughly 300 lattice parameters. The formation of a domain wall needs an additional amount of energy as the magnetic moments on the opposite sides of the wall change gradually from one easy axis orientation to another in neighboring magnetic domain by forcing magnetic moments to go through unfavorable energetically hard direction. Here the energy of exchange interaction between magnetic moments and anisotropy energy play important role. This overall extra energy required to form a domain wall is called Bloch wall energy per unit area. When a magnetic domain forms, the magnetostatic energy decreases, while wall energy increases. For a nanoparticle to split into domains, its size should be greater than the thickness of the domain wall. The subdivision process continues until the energy required to form a new domain wall is greater than the reduction in magnetostatic energy.

Further**,** as the dimensions reach nanoscale level, the energy reduction provided by multiple domains is overcome by energy cost of maintaining the domain walls and it becomes energetically favorable to form a single domain (SD), which is maximum size for such single-domain structures as depicted in Fig. 9, characterized by a critical size $D_C$ (or critical radius $R_C$). There is a term, pseudo single-domain (PSD) nanoparticles, which has been used for nanoparticles that fall in the overlap between nanoparticles that are well defined as being either single-domain and multi-domain behavior showing a region of large and small coercivity values, respectively [16]. When diameter of magnetic nanoparticle drops further down, the coercivity $H_c$ starts to drop gradually from its maximum value to zero, where a second major finite-size effect called

superparamagnetism (SPM) occurs. The superparamagnetism is characterized by another critical size $D_{SPM}$ as depicted in Fig. 9, and it is marked by a strong competition between the thermal fluctuations $k_BT$ and the uniaxial magnetocrystalline anisotropy energy $KV$ ($V$ is the volume of nanoparticle).

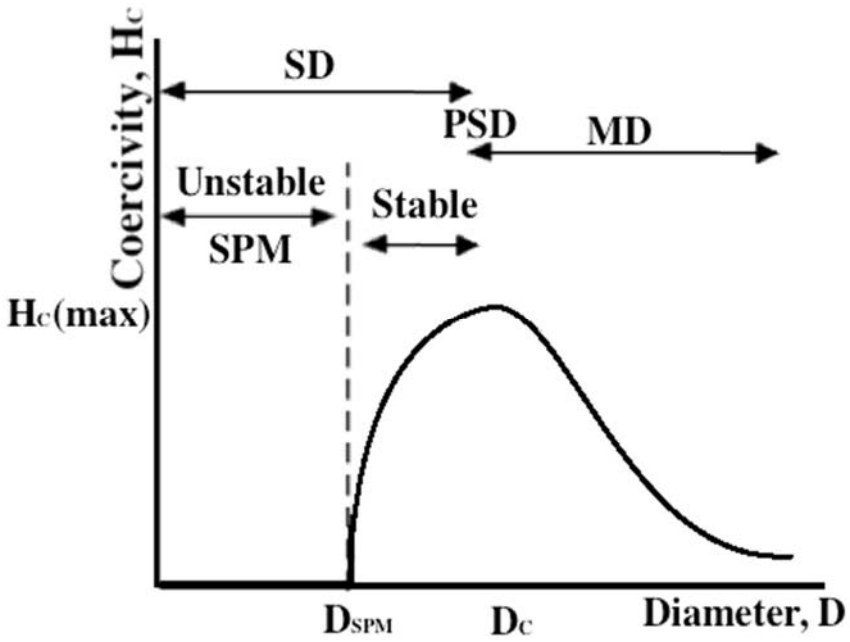


Fig. 9. Coercivity as a function of critical radius showing transition from superparamagnetic to single-domain to multi-domain regimes.

**COERCIVITY**

Coercivity or coercive field is the field required to force the magnetization to zero. From Fig. 9, coercivity increases with size but after reaching a maximum, decreases with size because as the size of magnetic nanoparticle increases, the nanoparticle become pseudo single-domain and then multi-domain structure in which the moment of each domain may not orient in same direction. On application of magnetic field, some of the non-parallel moments cancel, leading to reduced level of coercive field (coercivity). On the other hand, single-domain structure is uniformly magnetized with all spins aligned in the same direction. The magnetization will be reversed by spin rotation

since there are no domains to move. Due to this reason, single-domain particles show very high coercivity as it is harder to flip the magnetization than to move a domain wall [4].

**FLUX CLOSURE CONFIGURATION**

In this configuration, there is a formation of such a type of domains (e.g., triangular prism domains) with magnetization in one of possible easy axis directions which results in a complete enclosure of the magnetic flux within the volume of the ferromagnet with no magnetostatic energy. The boundaries of triangular prism domains near the end faces of the ferromagnet make an equal angle of $45^0$ with the magnetization of the domains (Fig. 10). As a result of it, the magnetization gradually rotates over a region which establishes 90° Bloch wall. Every Bloch

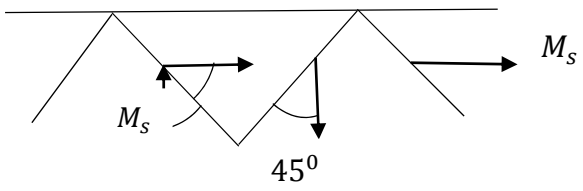


Fig. 10. Magnetic flux closure configuration [18].

wall formation needs energy. The most important contribution to its formation is due to anisotropy energy. Two of them are most important: magnetocrystalline and magnetoelastic anisotropy energies.

**MAGNETOCRYSTALLINE ANISOTROPY ENERGY**

The ferromagnet tends to be magnetized in certain easy directions of crystallographic axis due to magnetic anisotropy energy. To magnetize it in any other direction namely, a hard direction, additional energy called magnetocrystalline energy is required.

## MAGNETOELASTIC ANISOTROPY ENERGY

When a ferromagnet is magnetized in other than easy direction of magnetization, it causes the slight change in the lattice parameters. Since in flux closure configuration, the triangular prism or closure domains are magnetized along a different axis in comparison to the basic domains they tends to be elongated, making the lattice parameters longer in one dimension and shorter in other due to so-called magnetostriction. In order to fit the various domains together in a given volume some work has to be done against the elastic forces. So instead of changing the direction of magnetization some mechanical stress in the magnet are induced, which requires more energy to create the domain. This energy is called magnetoelastic anisotropy energy.

## MAGNETIZATION PROCESS

Domains in a ferromagnet can be magnetized in easy directions in such a way that it leads to overall magnetic flux completely enclosed in the volume of the sample. As a result of it, the resultant magnetization in the absence of an applied magnetic field is zero (Fig. 11a). By applying an external magnetic field, the resultant magnetization of the material can be created by increasing the volume of the domains which are favorably oriented with respect to the magnetic field at the expense of unfavorably oriented domains (Fig. 11b). This could be explained in terms of Zeeman energy. This energy due to interaction between magnetization and externally applied magnetic field is

$$E_H = -MH\cos\theta \tag{18}$$

where θ is the angle between the direction of applied field and magnetization M.

The domains with their magnetization vector close to the magnetic field direction are energetically favorable since they minimize interaction energy (Eq. (18)). Final magnetization process results

in the rotation of the most favorably oriented magnetization towards the direction of applied magnetic field (Fig. 11b).

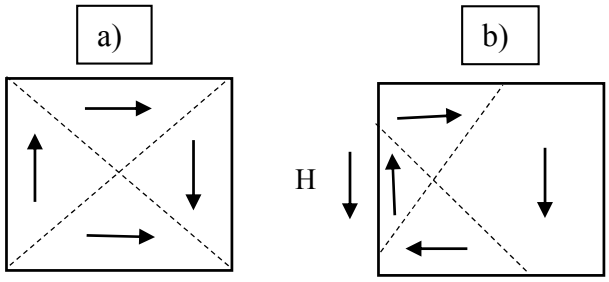


Fig. 11. Ferromagnetic domain configuration (a) with Bloch wall displacement and rotation of favorable magnetization vector (b) towards externally applied magnetic field direction.

## IV. CRITICAL SIZE OF FERROMAGNETIC NANOPARTICLES

We are looking for the critical radius of the ferromagnetic nanoparticle at which the energy of a single domain configuration is less than the energy of multi-domain structure. It can be done by finding the energies of each configurations and comparing these energies for different nanoparticle sizes. Let us consider magnetic configurations in spherical nanoparticles with a high and low anisotropy.

### ANISOTROPY ENERGY

The magnetization or magnetic moments per unit volume of ferromagnetic nanoparticles tends to be directed along certain crystallographic axes called directions of easy magnetization, which are energetically favorable directions. The directions along which it is most difficult to magnetize the material are directions of hard magnetization, which require a considerable amount of energy to magnetize it to reach its saturation. The excess of energy required to magnetize nanoparticles along the hard direction in comparison to easy axis direction is called anisotropy energy.

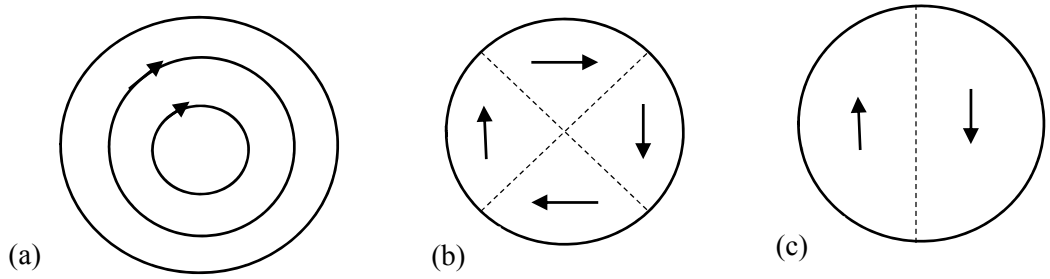


Fig. 12. Magnetic configuration for low anisotropy (a) and for high anisotropy in a cubic (b), and in a uniaxial (c) symmetry of magnetic nanoparticles [18].

### LOW ANISOTROPY

For low anisotropy, the circular magnetic configuration shown in Fig. 12a is the most energetically favorable flux closure configuration. Let us consider a circular ring of radius r inside a

nanoparticle. The corresponding magnetic moments (called spins from now on) which are located on the circular ring are separated by a lattice constant a. The total magnetic energy for a low anisotropy magnetic nanoparticle is mostly due to exchange energy (see, Eq. (19)) which results from the interaction between spins of two atoms. This is a quantum mechanical exchange interaction.

Number of spins n on the ring equals circumference of the ring divided by length of a side of unit cell a ($n = 2\pi r/a$). The exchange energy $W_{ex}$ includes interaction as the dot product between spins $\overrightarrow{\mathbf{S_i}}$ and $\overrightarrow{\mathbf{S_j}}$ as follows

$$W_{ex} = -\frac{1}{2}\sum_{ij} J_{ij}\ \overrightarrow{\boldsymbol{S_i}} \cdot \overrightarrow{\boldsymbol{S_j}} \tag{19}$$

where for all the (i, j) pairs of spins the factor ½ is introduced because the interaction between the same two spins is counted twice and $J_{ij}$ is the exchange integral constant for (i, j) pair of spins. If $\emptyset_{ij}$ is the angle between the pair, Eq.(19) can be written as

$$W_{ex} = -\frac{1}{2}\sum_{ij} J_{ij}\ S_i\, S_j\, cos\emptyset_{ij} \tag{20}$$

Let us assume that $|\overrightarrow{S_i}| = |\overrightarrow{S_j}| = |\vec{S}| = S$ and Eq.(20) can be written for the nearest-neighboring spins for large n as Eq.(21)

$$W_{ex} = -\,n\,JS^2 cos\emptyset \tag{21}$$

Expanding $cos\emptyset$ with respect to small angle $\emptyset$ between nearest neighbors only in Taylor series expansion and ignoring higher power of angles larger than two, we have (Eq. (22))

$$W_{ex} = nJ\ S^2\,\frac{\emptyset^2}{2} \tag{22}$$

According to Fig. 12a, the two spins represented as vectors are normal to the corresponding radius vectors. We can conclude that the angle between two spins is the same as the angle between two radius vectors of the ring making on the center of the ring (Fig. 13).

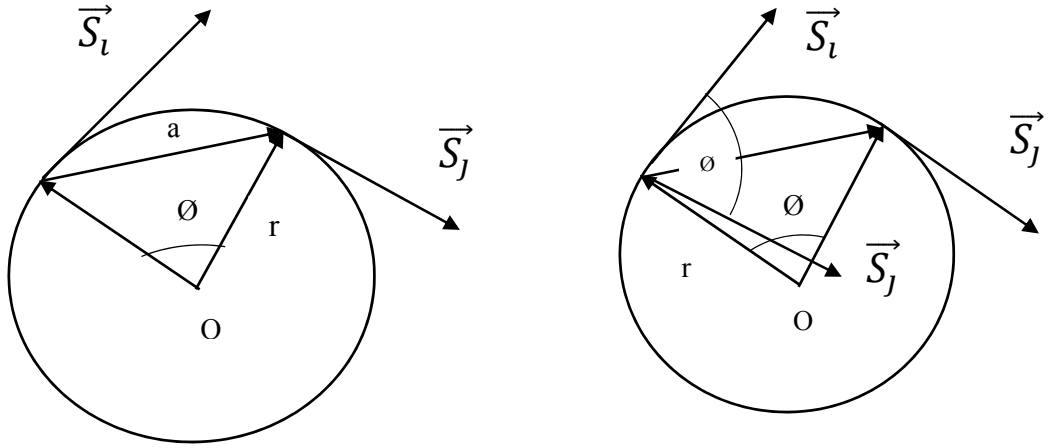


Fig. 13. Arrangement of nearest-neighboring spin vectors on a ring of radius r and angle ø between them.

Then the angle Ø between successive spins can be expressed as

$$\emptyset = \frac{a}{r} \tag{23}$$

The exchange energy of the ring in terms of angle $\emptyset$ and n = 2πr/a for S = 1 (for iron) can be expressed after straightforward calculations by Eq. (24)

$$W_{ring} = \pi J \frac{a}{r} \tag{24}$$

Now consider magnetic nanoparticle as a sphere which is made up of circular cylinders each one unit cell in thickness (see, Fig. 14). From Fig. 14c, the height of the cylindrical shell is given by Eq. (25)

$$D = 2\sqrt{R^2 - r^2} \tag{25}$$

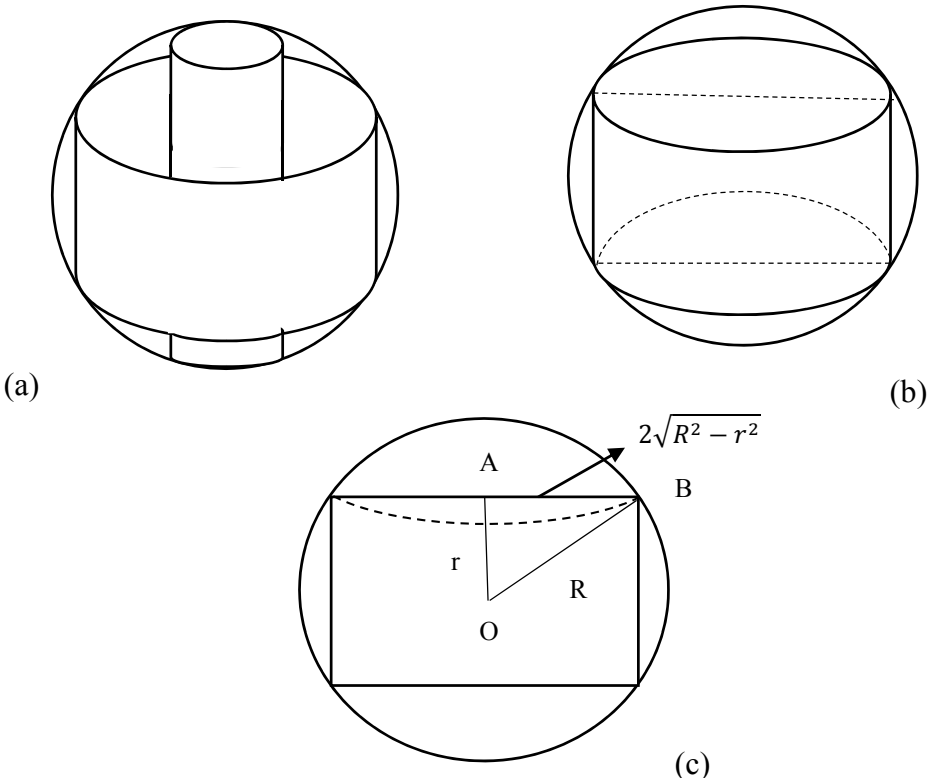


Fig. 14. Spherical magnetic nanoparticle with a couple of cylinders (a) and one cylinder (cylindrical shell) (b) and their geometrical parameters (c).

If each ring on a surface of the cylindrical shell is separated by lattice constant a then the total number of rings in the shell is given by Eq. (26)

$$N = D/a = (2/a)(\sqrt{R^2 - r^2}) \tag{26}$$

The magnetic energy of the interaction between spins on the cylindrical shell (see Eq. (27)) is given by the product of circular ring energy given by Eq. (24) and number of rings on the surface of cylindrical shell (Eq. (26))

$$W_{cyl} = N \bullet W_{ring} = 2\pi J(\sqrt{R^2 - r^2})/r \tag{27}$$

Total magnetic energy of spherical nanoparticles (constituting with cylindrical shells) can be obtained by integrating Eq. (27) with respect to r within the limit from a to R (see Eq. (28))

$$W_{ex} = \left(2\pi \frac{J}{a}\right) \int_a^R \left[\frac{\sqrt{R^2 - r^2}}{r}\right] dr = (2\pi JR/a) \left[ ln\left(\frac{2R}{a}\right) - 1\right] \quad (28)$$

The total magnetic energy density of nanoparticle with volume of the sphere $V_{sphere} = \frac{4}{3}\pi R^3$ is given by Eq. (29)

$$f_{ex} = \left(\frac{3}{2}\right)\left(\frac{J}{aR^2}\right) \left[ \ln\left(\frac{2R}{a}\right) - 1\right] \quad (29)$$

It can be seen from Eqs. (28) and (29) that magnetic energy and magnetic energy density of spherical nanoparticle depends on the radius R of nanoparticle. Now, we can estimate the values of total exchange energy of the spherical nanoparticle using Eq. (28) for different sizes of spherical nanoparticle. E.g., using the value $(J/a) = 2 \bullet 10^{-11}$ J/m, $S = 1$, and $a = 2.86 \bullet 10^{-8}$ m [18] for iron, we have $W_{ex} = 1.6 \times 10^{-11}$J when R = 1 cm and $W_{ex} = 35.3 \bullet 10^{-19}$ J when R = $10^{-6}$ cm.

**ENERGY OF SINGLE DOMAIN CONFIGURATION**

Let us consider a ferromagnetic nanoparticle of radius R as a single crystal in which there is regular arrangements of magnetic atoms in the form of cubic lattice. In the single domain configuration, the magnetic moments of the ferromagnetic nanoparticle are aligned in the same direction parallel to each other, giving rise to a large magnetic moment μ or saturation magnetization $M_S$. It means that this configuration has the largest possible magnetic moment for the nanoparticle of that size and composition. The magnetic moment in this case can be given as the product of the nanoparticle volume and the saturation magnetization $M_S$.

The total magnetic energy density of a single domain is mainly due to the magnetostatic energy density $f_D$ defined sometime as self-energy of the spherical ferromagnetic nanoparticle in its own

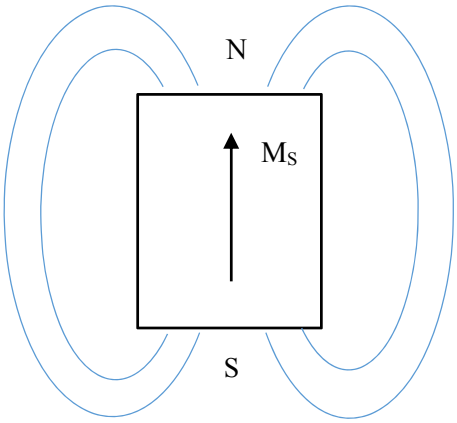


Fig. 15. Single-domain configuration.

field $H_D$ per unit volume (see, Eq. 30)

$$f_D = - H_D \bullet M_S/2 \tag{30}$$

where $H_D = - 4\pi M_S/3$ and Eq. (30) reduces to Eq. (31) which describes the total magnetic energy of the spherical nanoparticle

$$W_D = f_D \bullet V = 8\pi^2 M_S^2 R^3/9 \tag{31}$$

E.g., using the value $M_S = 1707$ G [18] for iron, we have $W_D = 2.5$ J when R = 1 cm and $W_D = 25 \bullet 10^{-19}$ J when $R = 10^{-6}$ cm. We can compare now the energy of single domain configuration and the energy of the simple domain arrangement for weak anisotropy for the spherical magnetic nanoparticle of radius R = 1 cm and $R = 10^{-6}$ cm.

We can conclude that when R = 1 cm, the energy of flux closure configuration has lower value than the single domain configuration. But for $R = 10^{-6}$ cm or 10 nm, the single domain configuration is energetically more favorable.

The equation for finding the critical radius $R_c$ of nanoparticle when transition takes place can be based on comparison of energies for the multi-domain and the single-domain configuration. Comparing Eq. (28) and Eq. (31), we can get Eq. (32) in terms of nanoparticle's radius R

$$\left(\frac{8\pi^2}{9}\right) M_s{}^2 R^3 = (2\pi JR/a)[\, ln\left(\frac{2R}{a}\right) - 1] \quad (32)$$

Eq. (32) will be solved later for $R_C$ numerically by using a program written in C++ language.

**HIGH ANISOTROPY**

So far we have discussed the case of low anisotropy and single domain configuration. For low anisotropy, the radius of magnetic nanoparticle is much smaller than the Bloch wall thickness. In the case of the high anisotropy material, the Bloch wall thickness is smaller than the radius of magnetic nanoparticle creating condition of the direct transition from the multi-domain structure to the single-domain configuration. In this section we will discuss two different crystallographic structures of magnetic nanoparticles: cubic and uniaxial symmetry (see, Fig. 12b and c).

**CUBIC CRYSTAL**

The important contribution to the total energy of magnetic nanoparticle in the case of high anisotropy is due to an energy needed to create Bloch wall (Fig. 16). The magnetic nanoparticle is large enough to create domain walls and more likely transition takes place between multi-domain and single-domain configuration directly. As it is well-known, the entire change in the spin direction between the oppositely magnetized domains (see, Fig. 16) does not occur in one discontinuous fashion across a single atomic plane but instead there is a gradual change in orientation over many atomic planes. The reason behind this is to minimize the exchange energy. The total energy of the nanoparticle for cubic symmetry (Fig. 12b) is due to entirely Bloch wall energy contribution and it equals (Eq. (33))

$$W_{wall} = 2\sigma_w \pi R^2 \quad (33)$$

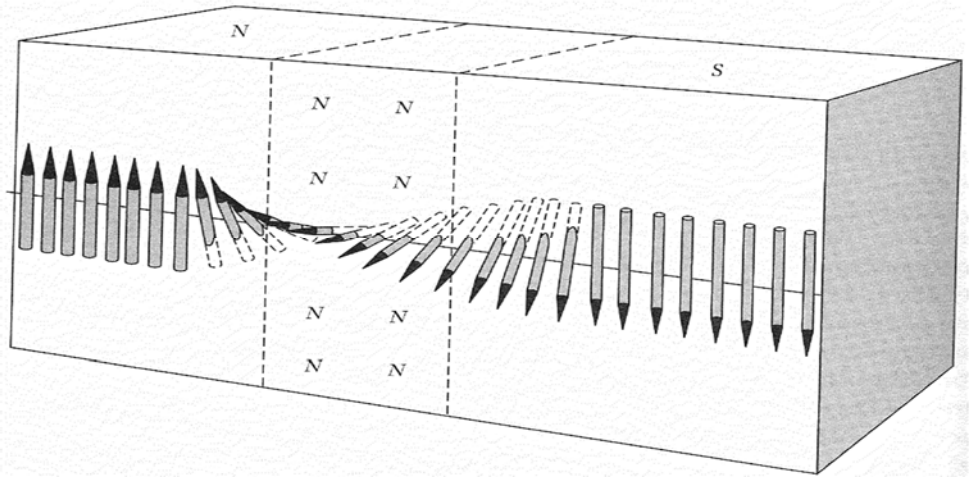


Fig. 16. Separation between two dotted planes representing Bloch wall thickness.

where R is the radius of the spherical nanoparticle, $\sigma_w$ is the Bloch wall energy per unit area of the wall and a factor two indicates the number of walls in this case (Fig. 12b). Let us assume N atom planes are contained within the wall, each of which is separated by lattice constant a. Thickness of the wall is equal to Na. The spins inside the wall are oriented away from the easy axis of magnetization with the hardest crystallographic axis in the middle of the Bloch wall. The total wall energy per unit surface is due to the contribution of two energies, exchange and magnetocrystalline anisotropy energy (see Eq. (34))

$$\sigma_w = \sigma_{ex} + \sigma_{anis} \tag{34}$$

where $\sigma_{anis}$ is the first order magnetocrystalline anisotropy energy per unit surface which is

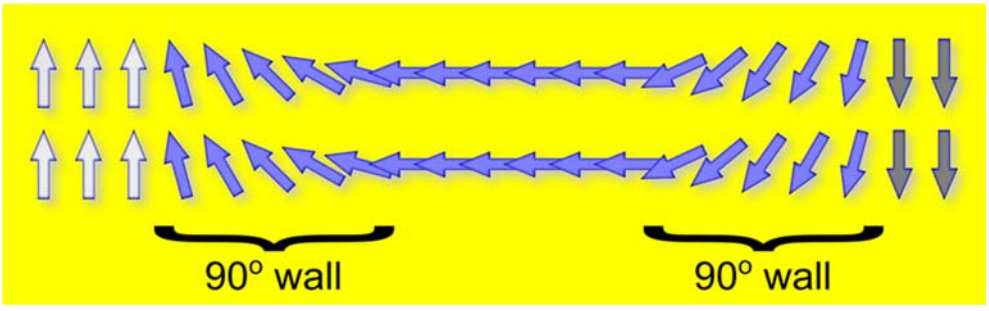


Fig. 17. $90^0$ domain Bloch wall.

approximately equal to

$$\sigma_{anis} \approx KNa \tag{35}$$

where K is the anisotropy constant and Na is Bloch wall thickness. The exchange energy between two spins making a small angle $\emptyset$ with each other has the form

$$W_{ex} = JS^2\emptyset^2/2 \tag{36}$$

where J is exchange integral constant and S is the spin measured in units of h/2π. Let the total change in angle between two neighboring domains be $\emptyset_0$ and if the change occurs in N equal steps then the angle $\emptyset$ in Eq.(36) would be $\emptyset = \emptyset_0/\mathrm{N}$. If $\emptyset_0 = \pi$ for $180^0$ Bloch wall and a change of angle occurs in N equal steps per unit surface area of $a^2$ then the exchange energy per unit area is given by

$$\sigma_{ex} = JS^2\pi^2/2Na^2 \tag{37}$$

By combining Eqs. (32), (35) and (37), the total wall energy per unit surface has the form

$$\sigma_w = \frac{JS^2\pi^2}{2Na^2} + KNa \tag{38}$$

and σw (Eq. (38)) has a minimum with respect to N when (see Eq. (39))

$$N = \sqrt{[JS^2\pi^2/2Ka^3]} \tag{39}$$

The total energy of the Bloch wall per unit area can be calculated by substituting value of N from Eq. (39) into Eq. (37)

$$\sigma_w = 3\pi\sqrt{JKS^2/2a} \tag{40}$$

For body centered cubic iron crystal, the Bloch wall thickness Na ≈ 300a and the total energy of the Bloch wall per unit area σw ≈ 1 erg/cm$^3$. The equation for the critical radius of nanoparticle

(see Eq. (41)) can be derived by using the fact that at the critical size the multi-domain structure makes transition to single-domain configuration based on the fact that energies for both configurations are equal at this critical radius. By comparing Eq. (31) with Eq. (33), we have

$$\left(\frac{8\pi^2}{9}\right) {M_s}^2 R^3 = 2\pi\sigma_w R^2 \tag{41}$$

which results in the following value for the critical radius of magnetic nanoparticle

$$R_c = \left({}^{9}/_{4\pi}\right)\left({}^{\sigma_w}/_{{M_s}^2}\right) \tag{42}$$

**UNIAXIAL CRYSTAL**

In uniaxial symmetry, the single-domain configuration is divided into two domains with antiparallel magnetization as shown in Fig. 12c. There is one easy axis of magnetization with two different orientations. At nanoparticle radius R, the total energy of single-domain configuration is equal to the energy of two-domain configuration (uniaxial configuration). The latter configuration (Eq. (43)) is equal to the sum of Bloch wall energy and half of the energy of single-domain configuration (Eq. (31))

$$W_{uni} = \pi\sigma_w R^2 + \left({}^{1}/_{2}\right)\left(\frac{8\pi^2}{9}\right) {M_s}^2 R^3 \tag{43}$$

By comparing Eq. (43) and Eq. (31), we end up with Eq. (44) for radius of nanoparticle in uniaxial crystal with a strong anisotropy

$$\pi\sigma_w R^2 + \left({}^{1}/_{2}\right)\left(\frac{8\pi^2}{9}\right) {M_s}^2 R^3 = \left(\frac{8\pi^2}{9}\right) {M_s}^2 R^3 \tag{44}$$

Solution of Eq. (44) with respect to R gives the value of critical diameter $R_c$ identical with Eq. (42).

## V. SURFACE EFFECTS

During the past decades, the size dependent properties of magnetic nanoparticles is of great interest which open wide research areas in most fields of science and engineering of nanometer sized materials and devices. Magnetic nanoparticles with unique physical properties have a high potential for the applications in diverse areas of high-density perpendicular recording, ferrofluids, ultrahigh frequency (300 MHz - 3 GHz) devices, and as a drug carriers for specific site drug delivery. These finite size effects become even more important in the case of high density data storage, floppy disk, and tape recording media because of the stability of information stored in the form of magnetized nanoparticles.

The magnetic properties will change when the bulk size material is reduced to nanometer scale. For instance, at low temperature, the saturation magnetization increases inversely with size due to the contribution from the densification and the localization of surface charges that contribute to the angular momentum of the lower-coordinated atoms whereas at room and high temperatures, saturation magnetization drops as the size is reduced because of the bond-order loss. This bond-order loss is also responsible for suppression of Curie temperature.

### SATURATION MAGNETIZATION

The saturation magnetization $M_S$ is defined as the maximum amount of magnetization achieved by magnetic material in the presence of large magnetic field at given temperature T. In late sixties Berkowitz et al [1] pointed out that at room temperature, saturation magnetization decreases with decreasing crystalline size due to the fact that the number of atoms on the surface is larger in comparison of the volume atoms. Due to the increase in the surface to volume ratio larger the fraction of atoms on the surface layer of the nanoparticle has the number of dangling exchange bonds between atoms as compared to the bulk system. These bonds are responsible for the

magnetic ordering below Curie temperature. Recently, Kodama et al. [19] proposed a disordered surface spin structure model to illustrate the low saturation magnetization of $NiFe_2O_4$ nanoparticles and Mamiya et al. [20] showed that low saturation magnetization of iron nitride ε-$Fe_3N$ nanoparticles is due to dipolar inter-particle interactions. In addition, Tang et al. [21] derived an empirical relation for size-dependent nature of saturation magnetization for a core-shell structure of magnetic nanoparticles. They assumed that the shell layer (non-magnetic layer) has a constant thickness and lower saturation magnetization as comparison to saturation magnetization of bulk material $M_{S0}$. The empirical relationship for size dependent $M_S$ is described by Eq. (45)

$$M_S(R) = M_{S0}\left(1 - \frac{\alpha}{R}\right) \tag{45}$$

where α is the fitting parameter, R is radius of nanoparticle and $M_{S0}$ is the saturation magnetization for bulk material. Moreover, the suppression of the saturation magnetization at room temperature was also interpreted as a result of the suppression of Curie temperature in the surface region as size reduces. Similarly, Nikolaev et al. [22] proposed a model for depression of Curie temperature (see Eq. (46)). This approach is based on the following assertion: the larger the fraction of atoms on the surface layer of the nanoparticle, the greater the number of loose exchange bonds between atoms as compared to large sized nanoparticle (as number of core atoms decreases). These bonds are responsible for the magnetic ordering below Curie temperature

$$\frac{T_C(R)}{T_{C0}} = 1 - \frac{\delta}{R} \tag{46}$$

where $T_{C0}$ is the Curie temperature for bulk material and δ is the fitting parameter, which depends on the size and signifies the number deficiency of the exchange bonds for the surface atoms of nanoparticle or thickness of the layer that is depleted of exchange bonds. Some literature suggests

that quantity δ is a parameter characterizing the influence of surface layer on the Curie temperature rather than the thickness of layer depleted of exchange bonds.

By incorporating the bond order-length-strength (BOLS) correlation mechanism into the Ising model and Brillouin function, both Curie temperature and saturation magnetization are determined by spin-spin exchange interaction energy $E_{ex}(R, T)$, which is proportional to the cohesive energy (see Eq. (51)). In terms of the BOLS correlation at room temperature $M_S(R)$

$$\frac{M_s(R)}{M_{s0}} = \alpha(J,T)\frac{E_{ex}(R)}{E_{ex0}} \approx 4\frac{E_{ex}(R)}{E_{ex0}} - 3 \tag{47}$$

$E_{ex}$ and $E_{ex0}$ is the exchange energy of nanoparticle and the bulk material, respectively. The parameter α(J,T) depends on temperature and the mean angular momentum J and e.g., α(J,T = 300K) = 4 for ferromagnetic nanoparticle at room temperature. However, the size effect on J is negligible compared with that of $E_{ex}$ at room temperature where $E_{ex}$ dominates the magnetic behavior. At very low temperatures, the magnetic moment increases compared to the bulk value due to the densification and localization of the surface charges that contributes largely to angular momentum of the lower-coordinated atoms and hence, it leads to the enhancement of saturation magnetization. Zhong et al. [23] developed a model to examine the temperature dependence of $M_S$ of ferromagnetic nanoparticles on R connecting suppression $M_S(R)$ to the decrease of the atom's cohesive energy $E_c(R)$ due to the coordination number imperfection of atoms near the surface edge. Most recently, $M_S(R)$ suppression at room temperature is also interpreted as a result of the Curie temperature $T_c$ suppression in the surface region [24].

Thermal (vibrational) energy $E_v(T_C) = k_B T_C$ required for disordering the exchange interaction $E_{ex}(R)$ is proportional to the cohesive energy $E_c(R)$ and therefore we have (Eq. (48))

$$\frac{T_C(R)}{T_{C0}} = \frac{E_c(R)}{E_{c0}} = \frac{E_{ex}(R)}{E_{ex0}} \tag{48}$$

$E_c(R)$ has been established to have the following form [25]

$$\frac{E_c(R)}{E_{c0}} = \left[1 - \frac{1}{\left(R/R_0\right)-1}\right] \exp\left[-\frac{2S_b}{R_g}\frac{1}{\left(R/R_0\right)-1}\right] \tag{49}$$

where $R_g$ is ideal gas constant, $R_0$ is the critical nanoparticle size at which solid and vapor phase is indistinguishable given by $R_0 = ch/4$ with h as the atomic or molecular radius, c is the constant $(0 < c \leq 1)$ and $S_b$ is bulk solid-vapor transition entropy given by Eq. (50)

$$S_b = H_v/T_b \tag{50}$$

where $H_v$ represents bulk solid-vapor transition enthalpy and $T_b$ is bulk solid-vapor transition temperature. From Eq. (49), we can see that $E_c(R)/E_{c0}$ decreases with decreasing R which reflects the instability of nanocrystal in comparison with the corresponding bulk. This trend is expected since the surface to volume ratio increases with decreasing size of nanoparticles. Fig. 18 shows $M_S/M_{S0}$ as a function of size for Fe, Co, and Ni ferromagnetic nanoparticles [25].

Taking into account Eq. (47), (48) and (49), and combining with Eq. (45), we get (Eq. (51))

$$\frac{M_S(R)}{M_{S0}} = \left(1 - \frac{\alpha}{R}\right) = 4\left\{1 - \frac{1}{(4R/ch)-1}\right\} exp\left\{-\frac{2S_b}{3R_g}\frac{1}{(4R/ch)-1}\right\} - 3 \tag{51}$$

Comparing Eq. (51) with Eq. (45), we can get an expression for fitting parameter α in terms of known parameters c, h, $S_b$, and $R_g$ (Eq. (52)) by using Taylor expansion and keeping its linear term only

$$\alpha = -4R\left\{1 - \left[\frac{1}{(4R/ch)-1}\right]\right\} exp\left\{-\frac{2S_b}{3R_g}\frac{1}{(4R/ch)-1}\right\} + 4R \approx ch(2 + \frac{4S_b}{3R_g}) \tag{52}$$

By using Eqs. (48), (49), and (46), the Curie temperature can be expressed as Eq. (53)

$$\frac{T_C(R)}{T_{C0}} = 1 - \frac{\delta}{R} = \left\{1 - \frac{1}{(4R/ch)-1}\right\} exp\left(-\frac{2S_b}{3R_g}\frac{1}{(4R/ch)-1}\right) \tag{53}$$

From Eq. (53), δ is as follows

$$\delta = R - R\left\{1 - \frac{1}{(4R/_{ch})-1}\right\} exp\left(-\frac{2S_b}{3R_g}\frac{1}{(4R/_{ch})-1}\right) = \alpha/4 \qquad (54)$$

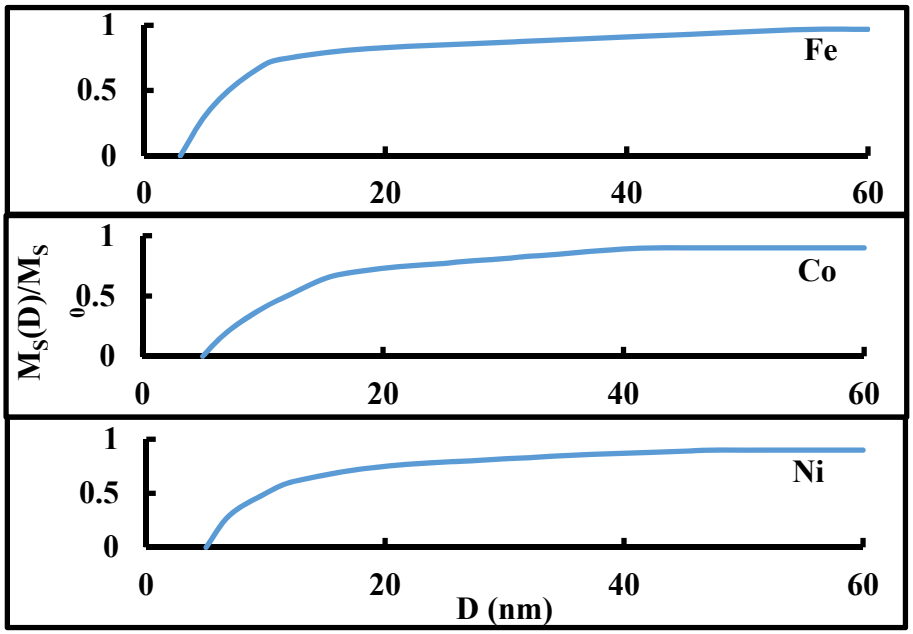


Fig. 18. Reduced saturation magnetization as a function of radius for (a) Fe, (b) Co, and (c) Ni ferromagnetic nanoparticles [26].

## SURFACE EFFECT ON ANISOTROPY

Surface effects in small magnetic nanoparticles are a major source of anisotropy because with decreasing particle size, the magnetic contributions from the surface become more important than those from the bulk of the particle. Surface anisotropy energy dominate over the magnetocrystalline anisotropy and magnetostatic energies. Many studies showed the increase in effective magnetic anisotropy due to surface effects. To the lowest order, the anisotropy energy of a ferromagnetic bulk sample [27] may be written as Eq. (55)

$$E_{anis} = K_o \sin^2\theta \qquad (55)$$

where θ is the angle between direction of magnetization and the easy axis, $K_o$ is the effective anisotropy constant. Experimental studies show that values of the effective anisotropy $K_{eff}$ is no longer inversely proportional to the volume as in the bulk but to the ferromagnetic nanoparticle's radius. In the case of single-domain spherical nanoparticles with radius R, effective magnetic anisotropy can be expressed as Eq. (60) and contribution from shape anisotropy is negligible as demagnetizing factors are isotropic in all directions [28],

$$K_{eff} = K_o + \frac{3}{R}K_s \tag{56}$$

where $K_s$ is the surface anisotropy constant.

**SURFACE EFFECT ON EXCHANGE INTEGRAL CONSTANT**

The exchange integral constant J as a function of radius R is given by Eq. (57) where $J_0$ is exchange integral constant for bulk material [29]-[30]

$$J(R) = J_0\left(1 - \frac{\beta}{R}\right) \tag{57}$$

where $J_o$ is the bulk exchange integral constant and β is the fitting parameter. $T_{c0}$ as the Curie temperature for the bulk is related to $J_0$ by the following relation (see Eq. (58)),

$$T_{c0} = \frac{2S(S+1)}{3k_B}J_0 \tag{58}$$

**SURFACE EFFECT ON CRITICAL SIZE OF FERROMAGNETIC NANOPARTICLES FOR LOW ANISOTROPY**

The critical radius of nanoparticles for low anisotropy was already discussed in Chapter III. The equation describing the critical size of ferromagnetic nanoparticles is given by Eq. (59)

$$\left(\frac{8\pi^2}{9}\right) {M_s}^2 R^3 = (2\pi JR/a)\left[\, ln\left(\frac{2R}{a}\right) - 1\right] \tag{59}$$

Eq. (59) can be rewritten by introducing surface effects in terms of fitting parameters α and β which leads to the new Eq. (60) in terms of nanoparticle's radius where $M_S(R)$ is replaced by Eq. (45) and J(R) is replaced by Eq. (57).

$$\left(\frac{8\pi^2}{9}\right)\left(M_{S0}\left(1-\frac{\alpha}{R}\right)\right)^2 R^3 \quad = J_0\left(1-\frac{\beta}{R}\right)(2\pi R/a)\left[ln\left(\frac{2R}{a}\right)-1\right] \tag{60}$$

A program in C++ to solve Eq. (60) (numerically with respect to R) has been written with the emphasis to find out the effect of surface parameters α and β on critical radius of nanoparticle.

## VI. HEAT MECHANISMS IN FERROMAGNETIC NANOPARTICLES

Heat generation in magnetic nanoparticles in the presence of externally applied magnetic field can be ascribed to one of three different mechanics, depending on size as described below. A material's magnetic behavior can change as its dimensions approach the nanoscale range and this also affects the heating (loss) mechanism in an alternating magnetic field. When ferromagnetic nanoparticles are irradiated with an alternating magnetic field they transform the energy of field into heat using the following four mechanisms:

- hysteretic loss in bulk and multi-domain ferromagnetic nanoparticles,
- relaxation losses in superparamagnetic phase,
- frictional loss in viscous suspensions,
- Eddy current loss.

### HYSTERESIS LOSSES

In the previous Chapters we discussed concept of domain formation and magnetization mechanism in magnetic nanoparticles in details. Hysteresis loss is related to one of magnetization mechanism. Typical ferromagnetic nanoparticles demonstrate unique regions of magnetization known as magnetic domains, separated by narrow zones of transition termed as domain walls. Domains forms to minimize the overall magnetostatic energy of the material but as the dimensions reached nanoscale level, the energy reduction provided by multiple domains is overcome by energy cost of maintaining the domain walls and it becomes energetically favorable to form a single domain. Hysteresis loss can occur in single-domain and multi-domain nanoparticles. When exposed to an externally applied field, the magnetic material tends to align in the direction of applied field. Most of the time, domain walls can move in the presence of applied field in a way that many single domain combine and create larger domain which is known as domain growth. It can be explained

that domains whose magnetic moments are favorably oriented with respect to the applied field increase in size on the expense of domains whose magnetic moments are unfavorably aligned with respect to the field. This domain wall displacement continues until saturation magnetization $M_S$ is reached, at which the domain walls are maximally displaced. This domain wall displacement (response of domain wall to an alternating magnetic field) is shown in Fig. 19 (also see Fig. 11b).

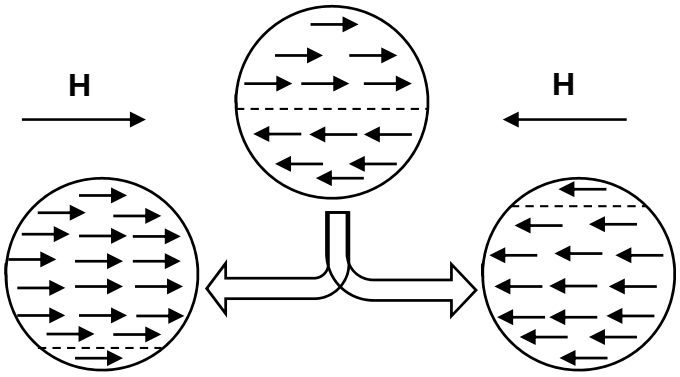


Fig. 19. Domain wall displacement in the presence of applied magnetic field.

The relationship between applied magnetic field and magnetization is shown in Fig. 20. This magnetization curve is referred as hysteresis loop for all strength of applied magnetic field. For increasing values of applied magnetic field strength, the magnetization will increase up to saturation level. This limit of an extremely large magnetic field gives rise to saturation magnetization, when all domains are oriented parallel and points in same direction. We call this first curve as a virgin curve. If the magnetic field is now reduced, the plot will follow a different path that lies above the initial magnetization curve. This is due to a delay in demagnetization. It is said that there is a hysteresis. If then magnetic field is further reduced back to zero field strength, magnetization curve will be offset from the original curve (curve lags behind the original curve) by an amount known as remanent magnetization $M_r$ or remanence. If a field in opposite direction

is applied, magnetization will reach a null point at the coercive force $H_c$. The width of the middle section of the loop describes the amount of hysteresis, related to the coercivity of the material. As a whole, if the magnetic field applied to a ferromagnetic material is first increased and then decreased back to its original value, the magnetic field inside the material does not return to its original value but lags behind the externally applied field. This process results in loss of energy in the form of heat. This loss is due to the friction of magnetic domains when changing direction. Indeed, the magnetization of the material absorbs energy which is only partially restored during demagnetization. The amount of energy dissipated or heat generated is directly related to the area of hysteresis loop [15]. The area of hysteresis loop $A_{Hys}$ is given by Eq. (61)

$$A_{Hys} = \oint HdB \tag{61}$$

where H is the magnetic field and B is the magnetic induction, $B = \mu_0(H + M)$, $\mu_0$ is the permeability of free space and M is magnetization. By rearranging Eq. (61), we have

$$A_{Hys} = \mu_0 \oint Hd(H + M) = \mu_0 \oint HdM \tag{62}$$

This area is equal to the amount of energy dissipated. If the process of magnetization and demagnetization is repeated f times per second, we will get hysteresis power loss $P_{Hys}$

$$P_{Hys} = \mu_0 f \oint HdM \tag{63}$$

**NEEL AND BROWN RELAXATION LOSSES**

There are two types of relaxation losses which occur in superparamagnetic nanoparticles and lead to heat generation in this regime. These losses fall into two categories: Brownian and Neelian (see Fig. 21). The Brownian relaxation represents the rotational frictional component in a given suspending medium when the nanoparticle tries to align with the externally applied field. As the

whole particle oscillates towards the field, the suspending medium opposes this rotational motion which results in heat generation. It implies that Brownian motion is due to orientation fluctuations

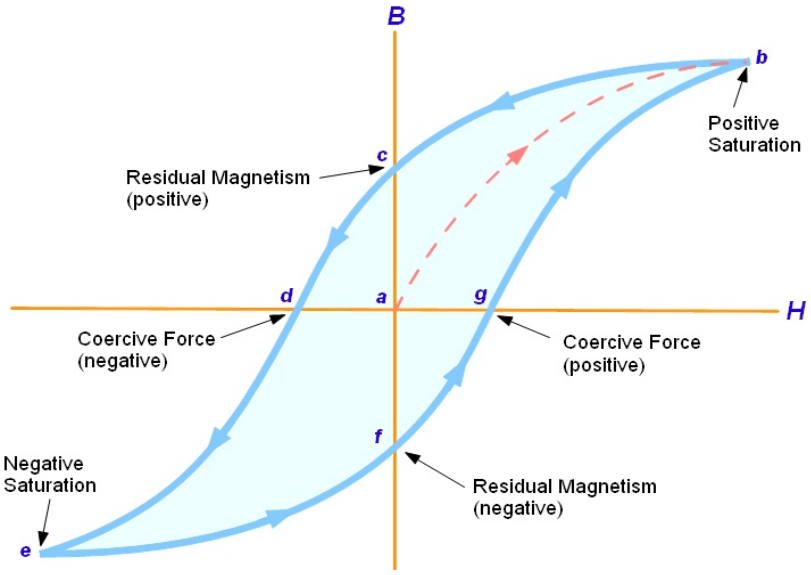


Fig. 20. Hysteresis loop.

of nanoparticle itself in suspending medium, assuming the magnetic moment is locked onto the crystallographic anisotropy axis. The time taken by the magnetic nanoparticle to align with the externally applied magnetic field is known as the Brownian relaxation time $\tau_B$ given by Eq. (64)

$$\tau_B = \frac{3\eta V_H}{k_B T} \tag{64}$$

where $\eta$ is the fluid viscosity and $V_H$ is the hydrodynamic volume of the nanoparticle (including coatings).

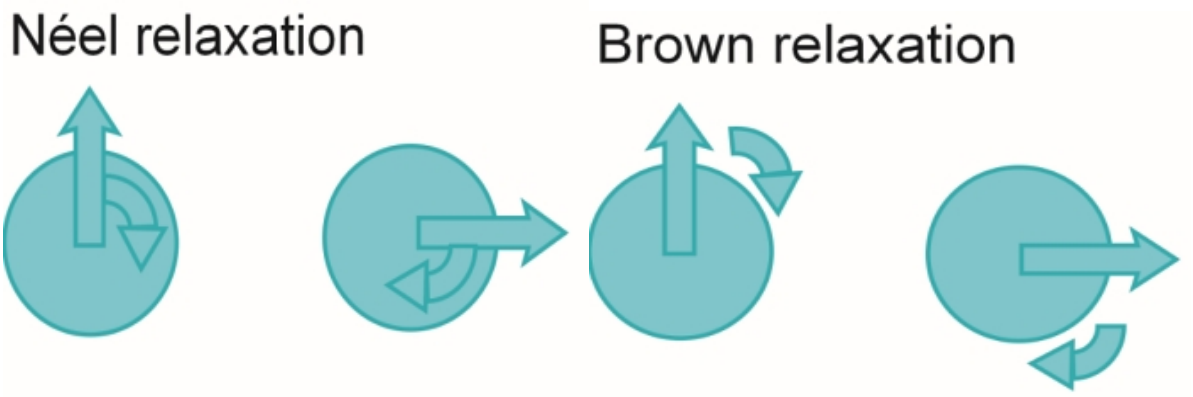


Fig. 21. Neel and Brown relaxation processes.

The Neel relaxation represents the rotation of the individual magnetic moments in the direction of the external magnetic field. In the presence of an external field, the magnetic moment rotates away from the crystal axis towards the field to minimize potential energy. The remaining energy is then released as heat into the system. It implies that Neel relaxation is due to the internal rotation of the nanoparticle's magnetic moment, which occurs when the anisotropy energy is low compared to the thermal energy. The typical time between orientation changes is known as Neel relaxation time $\tau_N$ given by Eq. (65). Neel relaxation time $\tau_N$ occurs also when nanoparticle movement is blocked.

$$\tau_N = \frac{\sqrt{\pi}}{2}\tau_0 \frac{e^{\frac{KV}{k_B T}}}{\sqrt{\frac{KV}{k_B T}}} \tag{65}$$

where $\tau_0$ is the attempt time (generally $10^{-9}$ sec), V is the volume of ferromagnetic nanoparticle, $k_B$ is Boltzmann's constant, K is the nanoparticle anisotropy constant, and T is the absolute temperature. As the two relaxation processes are occurring simultaneously, there is an effective relaxation time given by $\tau$ (see, Eq. (66)).

$$\tau = \left(\frac{1}{\tau_N} + \frac{1}{\tau_B}\right)^{-1} = \frac{\tau_N \tau_B}{\tau_N + \tau_B} \tag{66}$$

From Eq. (64), it can be seen that Brown relaxation time varies with to the radius of the nanoparticle and fluid viscosity while Neel relaxation time depends, in much more complicated fashion, on the radius of the nanoparticle and the magnetic anisotropy energy. Relative relaxation mechanisms for iron (K = 43 kJ/m$^3$) nanoparticles in water (low viscosity η = 0.0009 kg/m•sec) are represented in Fig. 22. The effective relaxation time is represented by a blue line while time for Neel relaxation and Brownian relaxation are represented by red and dashed line, respectively. The crossover between Neel and Brown regime corresponds to maximum value of heat (known as specific absorption rate (SAR)) which occurs roughly at a critical radius of the order 5.5 nm and relaxation time is of the order of $10^{-6}$ sec.

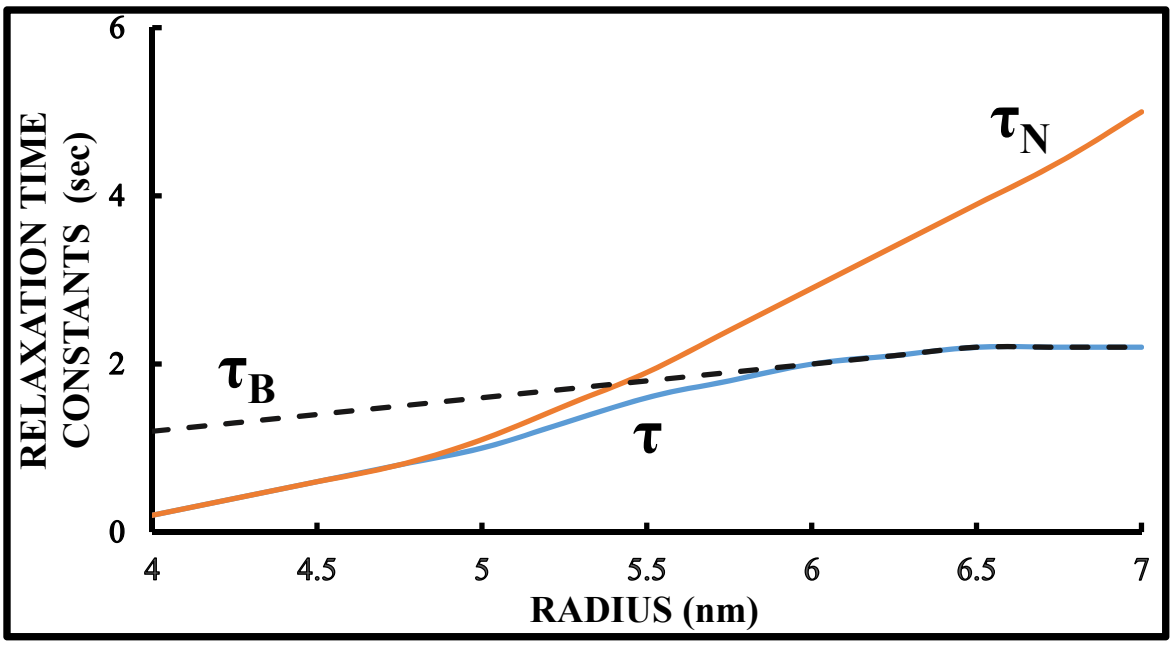


Fig. 22. Effective relaxation time for iron as a function of the radius of the nanoparticles in water with a 2 nm magnetic coating at T = 300 K [31].

It is clear that Neel relaxation time depends upon the anisotropy constant, which is material dependent. In order to achieve maximum heat, in the range of preferred excitation frequencies there is an ideal core size for Neel contribution [31]. Heating response has a strong dependence on

viscosity of surrounding medium. An increase in the viscosity produces longer Brownian time constant. As a result, particle rotation may be slow and this can decrease or eliminate Brownian contributions. As in our case, we used water as suspending medium which has low viscosity, so it can be said that Brownian contribution towards the heat generation may be prominent. It can be seen from the graph that in the range of 4 < R < 6 nm, Brownian contribution is prominent while in the range of 6 < R < 8 nm, Neel contribution is prominent. The total volumetric power generation P known as power loss density is given by Eq. (67)

$$P = \mu_0 \chi'' \pi H_0^2 \bullet f \tag{67}$$

where $H_0$ is the intensity of ac magnetic field, f is the frequency of the applied field and $\mu_0$ is the magnetic susceptibility of vacuum. The frequency dependence of relaxation of the nanoparticle ensemble can be given through the complex susceptibility. The magnetic susceptibility is $\chi = \chi' - i\chi''$ with $\chi'$ is the in-phase (real) component and $\chi''$ is the out-of-phase (imaginary) component. This susceptibility is dependent on both nanoparticle and magnetic field parameters and given by Eq. (68)

$$\chi'' = \frac{\chi_0 \varphi}{1+\varphi^2} \tag{68}$$

where $\chi_0 = M_S^2 V/k_B T$ is known as static susceptibility $\varphi = f \bullet \tau$ is known as ferrofluid volume fraction. At low frequencies ($\varphi << 1$), i.e., in the superparamagnetic regime, the losses increase with the square of frequency as given by Eq. (69)

$$P = \mu_0 \chi_0 \pi H_0^2 \bullet f^2 \tau \tag{69}$$

while for ($\varphi >> 1$) losses saturate and become independent of frequency Eq. (70)

$$P = \frac{\mu_0 \chi_0 \pi H_0^2}{\tau} \tag{70}$$

The SAR for monodisperse nanoparticles (no variation in size) can be expressed in terms of volumetric power generation P given by Eq. (71)

$$P = (\mu_0 \pi f H_0^2)\left(\chi_0 \frac{f\tau}{1+(f\tau)^2}\right) = SAR \tag{71}$$

This is the power delivered to the environment where the ferromagnetic nanoparticles are placed. The very strong size dependence of the relaxation time leads to a very sharp maximum of the loss power density in dependence on nanoparticle size. Accordingly, a remarkable output of heating power occurs only for nanoparticle systems with narrow size (and anisotropy) distribution and with the mean diameter being well adjusted in relation to the treated frequency [32]. Therefore, the highest heating power output can be achieved only for careful adjustment of field parameters (frequency f and amplitude $H_0$) in accordance with nanoparticle properties (size and anisotropy).

**FRICTIONAL LOSSES**

The Brown mechanism causes generation of heat as a result of viscous friction between rotating nanoparticles and surrounding medium. This type of loss is not restricted to superparamagnetic nanoparticles. In general, nanoparticles which may be regarded as small permanent magnets with remanent magnetization $M_R$ and volume V are subject to a torque moment, when exposed to an oscillating magnetic field H (see, Eq. (72))

$$\tau = \mu_0 M_R H V \tag{72}$$

In the steady state, the viscous drag in the liquid $12\pi\eta Vf$ is counteracted by the magnetic torque $\tau$ and the loss energy per cycle is simply given by $2\pi\tau$ [32]. The effect of viscous losses was clearly demonstrated in experiments with relatively large (~100 nm) crushed magnetite nanoparticles suspended in an aqueous sol containing commercial gelatine which is stiff below about $30^0$C and liquid at higher temperatures. On heating above the melting point the specific loss power increases

by nearly an order of magnitude up to 200 W/g at a field amplitude of 6.5 kA/m and a frequency of 410 kHz [32].

**EDDY CURRENT LOSSES**

Eddy current induction takes place whenever a conductor is exposed to an alternating magnetic field and result in resistive heating. Significant eddy current heating is observed only for bulk magnetic materials. Heating induced by eddy currents is negligible in comparison to the purely magnetic heating generated by magnetic nanoparticles since the heating power decreases with decreasing diameter of the conducting material.

## VII. SYNTHESIS AND CHARACTERIZATION OF FERROMAGNETIC NANOPARTICLES

Magnetic iron-oxide nanoparticles have very large surface-to-volume ratio and therefore possess high surface energies. Such nanoparticles tend to form agglomerates to reduce the surface energies. Moreover, the iron oxide nanoparticles are easily oxidized in air, resulting in loss of magnetism and dispersibility [33]. Therefore, it is important to have a proper surface coating and some strategies to develop effective protection to keep magnetic nanoparticles stable. This can be achieved by grafting of or coating with organic molecules like small organic molecules or surfactants, polymers and biomolecules or coating with inorganic layers like silica, metal or nonmetal elementary substance and metal oxides [33]. The interaction between surfactant and the nanoparticle is important for the synthesis of magnetic nanoparticles as the magnetic structure of the surface layer is well different from the nanoparticle and the magnetic interaction in the surface layer could have a notable effect on the magnetic properties of nanoparticles [33]. Oleic acid (OA) is commonly used as a surfactant.

There are various methods for the synthesis of magnetic nanoparticles like water-in-oil microemulsion, polyol, gas deposition, co-precipitation, sol-gel, pyrolysis, thermal decomposition of organic iron precursor, hydrothermal and others. Every method has specific procedure and conditions, and magnetic nanoparticles of different properties can be synthesized using these methods [34].

### FERROMAGNETIC NANOPARTICLES

Iron nanoparticles (Fe) were prepared by thermal decomposition of iron precursor method in Cambridge University, United Kingdom by group supervised by Andrew Wheatley [35]. During our work, we are mainly concerned with iron nanoparticles. Thermal decomposition method is used for the synthesis of highly monodispersed nanopararticles. During this method, some organic

iron compounds like (hydroxylamineferron [Fe $(Cup)_3$], iron pentacarbonyl [Fe $(CO)_5$], ferric acetylacetonate [$Fe(acac)_3$], iron oleate [$Fe(oleate)_3$] are decomposed at high temperature inside the non-polar boiling solvent with a presence of the capping agent [34]. The main magnetic material used in this research is iron nanoparticles. Iron is a magnetic material with a high magnetic moment density of 220 emu/g [37] and high saturation magnetization of bulk iron is 218 $Am^2/kg$ [35] and is magnetically soft [38]. Its heat capacity at 293 K is 0.4504 J/$^0$Cg. It is by mass the most common element on Earth. The inner and outer core of Earth is made up of iron. Iron oxidizes to give two iron oxides: magnetite ($Fe_3O_4$) and maghemite ($\gamma$-$Fe_2O_3$). Magnetite's IUPAC name is iron (II or III) oxide and contains divalent and trivalent Fe ions with black or grayish black color. Saturation magnetization of bulk magnetite material at 25$^0$C is 90-92 emu/g [34]. Magnetite is sensitive to oxidation and oxygen transforms it to maghemite by oxidation of $Fe^{2+}$ ions. Maghemite's IUPAC name is iron (III) oxide and contains only trivalent Fe ions with brown color. Saturation magnetization of bulk maghemite material at 25$^0$C is approximately 80 emu/g [34]. Sizes of different iron nanoparticles used in this work are summarized in Table I.

**IRON NANOPARTICLES' PREPARATION**

Chemical reactions were carried out under an argon atmosphere using standard air sensitive techniques. Synthesis procedure and scheme involved for iron nanoparticles is as follows:

iron nanoparticles were synthesized by thermal decomposition of iron pentacarbonyl [$Fe(CO)_5$] in the presence of oleic acid (OA)/octyl ether (OE) or PVP (Scheme). Solutions of [$Fe(CO)_5$] were injected into mixtures of capping agent at 100°C and the mixtures were heated to reflux. Surfactant concentration and reflux time were adjusted in order to obtain nanoparticles of specific size. The reaction mixture was cooled to room temperature and Fe nanoparticles were separated by the addition of ethanol followed by centrifugation.

Table I. Average sizes of iron nanoparticles [37].

| Nanoparticles | Diameter D (nm) |
|---|---|
| Fe9 | 5.94 ± 1.27 |
| BKFe10 | 7.97 ± 1.52 |
| BKFe15 | 10.31 ± 1.83 |
| BKFe20 | 18.31 ± 1.95 |
| BKFe25 | 18.61 ± 1.97 |
| PTFe2 | 21.44 ± 1.73 |
| PTFe3 | 12.61 ± 1.62 |
| PTFe4 | 21.44 ± 1.73 |
| PTFe5 | 20.43 ± 1.42 |
| PTFe7 | 21.40 ± 1.50 |

Re-dispersion was carried out in an organic solvent and then creating a powder followed.

$$Fe(CO)_5 \xrightarrow{\text{OA, OE, reflux}} \text{Co NPs} + 5CO$$

Scheme: Fe nanoparticle formation (OA = oleic acid, OE = octyl ether)

**NANOPARTICLES' CHARACTERIZATION**

Probably the most powerful technique for characterizing nanomaterials is Transmission Electron Microscopy (TEM). Using this technique, we can image nanoparticles in the nanometre size scale. Among different kinds of TEM, low resolution TEM and high resolution TEM are the most commonly used for analysis of nanoparticles. Low resolution TEM provides a basic image of the nanoparticles which helps to find statistical measurement of size and shape of nanomaterials. High resolution TEM helps us to elucidate the internal lattice structure of each nanoparticle. TEM can also help determine the crystal structure of a nanomaterial through selected area electron diffraction technique [36]. In this work, nanoparticles were characterized using a JEOL JEM-3011 HRTEM (high-resolution Transmission Electron Microscopy) at nominal magnifications of

x100k-x800k [35]. Nanoparticle size distributions were analyzed by counting the diameters of 100 nanoparticles in the lower magnification images, then defining size intervals of 0.2 nm between $D_{min} \leq D \leq D_{max}$, and counting the number of nanoparticles falling into these intervals. This data was then used to construct nanoparticle size distributions using Data Graph 3.0 [35].

## VIII. EXPERIMENTAL SETUP FOR MEASUREMENT OF HEATING RATE AND SPECIFIC POWER LOSS

In this Chapter, we are going to discuss the experimental setting for measurements of heating rate of nanoparticles. In this project, since nanoparticles are irradiated by an alternating magnetic field and they liberate heat to their surroundings, which is water in present case. So, the measurements of the temperature of nanoparticles accurately are very important in order to find out the heat released by particular amount of nanoparticles. This heating performance of nanoparticles is described in terms of Specific Power Loss (SPL) or Specific Absorption Rate (SAR) which depends on the rate of change of temperature. Different amount of nanoparticles release different quantity of heat to the environment. This difficulty was eliminated by using the same quantity of nanoparticles with the same amount of water added every time. So, the accurate measurement of the mass of nanoparticles and water used is really important. Based on the above requirements and proper measurements of the heating rate of nanoparticles when irradiated by a magnetic field, the system consists of a function generator, a current supply, a power supply, a chiller, a coil, a temperature probe, a vacuum pump and a very accurate mass balance. Each of these parts are explained in details in following sections.

### TEMPERATURE PROBE

Temperature measurement is the prime parameter for the determination of SAR values. The temperature probe used should have a high degree of precision, accuracy and almost instantaneous response without effecting the medium whose temperature is being measured. The temperature probe used in this project is FISO Inc. FOT-L Temperature Sensor. This temperature sensor has following characteristics [39].

1. It is fiber-optics temperature sensor which enables accurate, stable and repeatable measurements of temperature. It has an accuracy of .0001 K.

2. It has a Fabry-Parot cavity constituted by two optical fibers precisely assembled into a glass capillary. The length of the cavity changes with temperature variations due to the difference in the coefficient of thermal expansion between optical fiber and the glass capillary.

3. The temperature measurements are based on variations of the reflected light. When compared to the emitted light due to thermal expansion of the glass used within the sensor.

4. It is immune to EMI and RFI since the sensors are not electronically active. Hence they do not emit nor are they affected by any EM radiations and weather.

5. It has miniature size and microscopic contact area so it can be inserted even if the apparatus does not support temperature sensing inherently. Also, due to small size of the sensor, the thermal inertia is virtually reduced, which allows ultra-fast temperature monitoring.

6. It is sheathed with PTFE and has a temperature range from as low as −40°C up to 300°C (−40°F to 572°F).

7. It has a very low heat capacity so it does not give in or take heat to the material and there will be no effect on the temperature of the material being measured.

8. The structure of the sensor has an influence on minimum amount of the sample needed to assure that the sensitive part of the sensor was imbedded in the sample.

9. It offers accuracy and reliability in extreme temperature and hostile environmental conditions.

10. The fiber optic lead cable can be up to several meters long without affecting the quality or the accuracy of the results.

Specifications of FOT-L temperature sensor are summarized in Table II and Fig. 23 shows FOT-L temperature sensor.

Table II. Specification of FOT-L temperature sensor.

| | |
|---|---|
| Temperature range | 40°C to 250°C |
| Resolution | 0.001°C |
| Accuracy | 0.01°C |
| Response time | ≤ 0.5s |

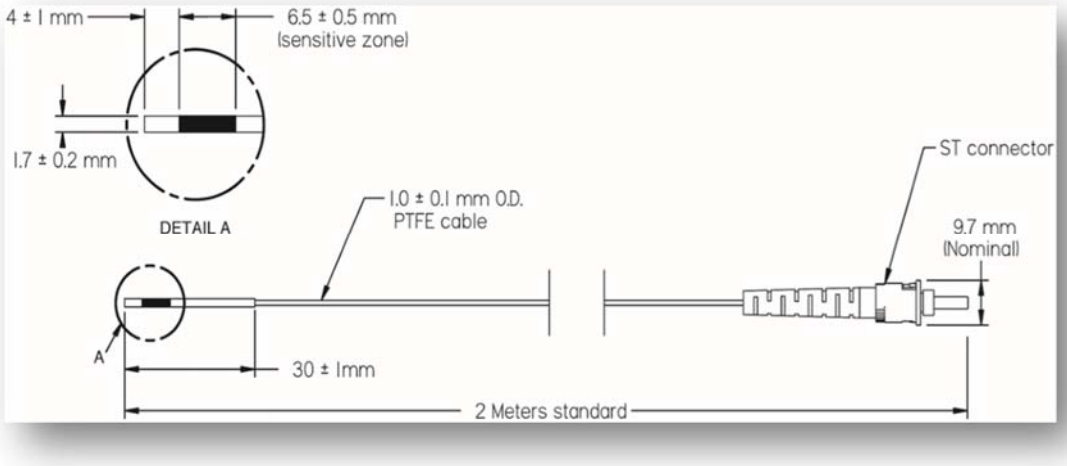


Fig. 23. FOT-L temperature sensor [39].

**FREQUENCY OF OPERATION**

The heating of magnetic nanoparticles whether ferromagnetic or surerparamagnetic nanoparticles depends how fast the magnetic field is changing with time. These time varying magnetic fields have a direct effect on human tissues and can cause nerve simulations and effect the neurological functioning of the human body [40]-[44]. So, setting a frequency range for the heating measurements is a vital part of the experiment. A higher frequency will produce a higher temperature raise in magnetic nanoparticles but this frequency should be safe for human tissues. Also, heating mechanism is different at low frequency (f <100 kHz) from that of high frequency (f > 100 kHz). The low radio-frequencies are defined as the frequencies between 300Hz and 100 kHz. They involve two different phenomena's of induced currents and dielectric absorption which cause stimulation of muscle cells. On the other hand, at high radio-frequencies, tissue heating is

the main mechanism due to the ability of the magnetic energy of high radio-frequency oscillating field to heat biological tissues very rapidly. As human tissue is not able to withstand the excessive heat generated by this thermal effect and thus eventually damage themselves during the exposure to high RF levels. Two areas of the body, eyes and testes, are particularly vulnerable to heating because of the relative lack of available blood flow to dissipate the excessive heat load. Keeping all these effects in mind, three different frequencies of 88 kHz, 130 kHz and 175 kHz were used as the operating frequencies for this project.

**MAGNETIC FIELD AND CUSTOM COIL**

In order to produce a uniform magnetic field around the sample, a custom made coil in the form of a solenoid was used. A regular solenoid consists of wires wrapped around each other in such a way that it produces a constant and uniform magnetic field inside when electric current is applied. The magnetic field of an infinitely long solenoid is given by Eq. (73)

$$B = \mu NI/L = \mu nI \tag{73}$$

where, n = N/L is number of turns per unit length of the solenoid [45]. The magnetic field strength does not depend on the distance from the axis or on the cross-sectional area of the solenoid in comparison to the magnetic field generated by a single current carrying wire, whose strength is inversely proportional to the distance from the center of the wire [46]. Fig. 24 shows pattern of magnetic field lines in a solenoid of the finite length. A custom-made coil with diameter of 3 cm and length of 4 cm and consists of insulated copper sheets wrapped around each other 20 times in the form of a spiral solenoid was used.

**POWER SUPPLY AND FREQUENCY GENERATOR: AMF SYSTEM**

The custom-made power supply (black box) is used for the production of an alternating current at the range of kilohertz. This alternating current is fed to the custom coil.

The variable frequencies fed by a frequency generator with custom made power supply are shown in Fig. 25.

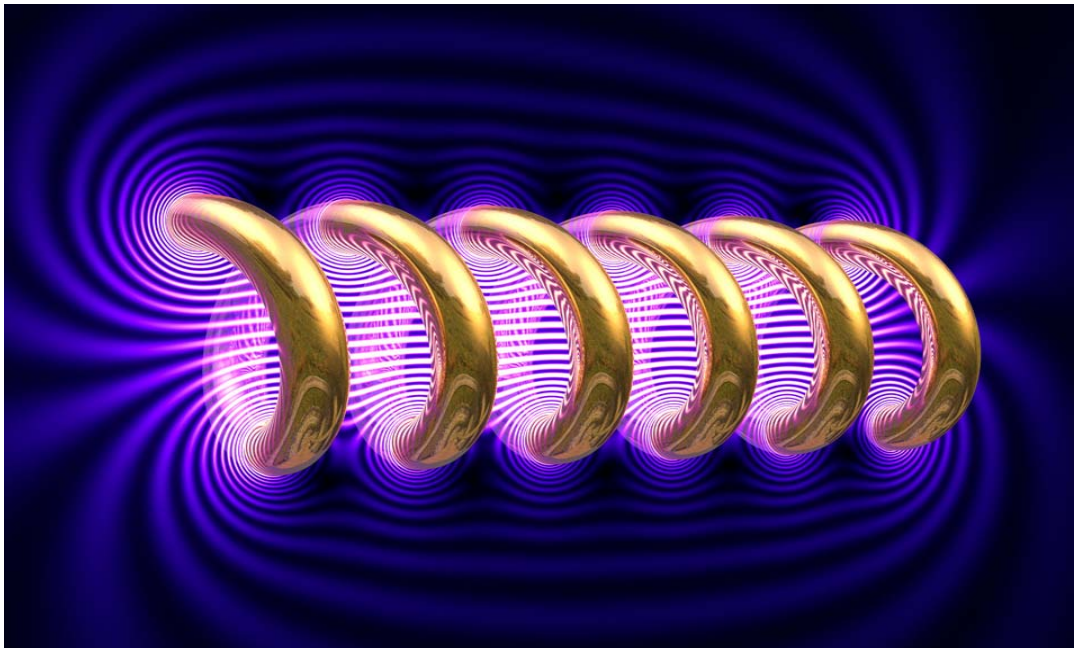

Fig. 24. Magnetic field of finite length solenoid (3-D image) by Paul Nylander [47].

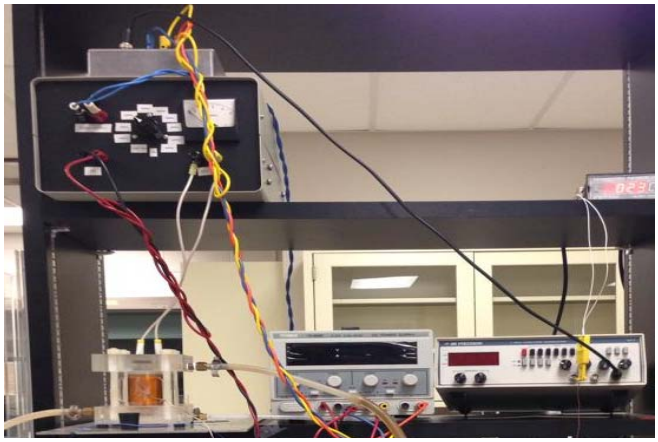

Fig. 25. Black box of custom-made power supply and frequency generator.

An external frequency generator was used to fine tune the resonant frequency of the system. The frequency generator was manufactured by BK Precision and named as BK Precision 4011A

function generator. It is able to sweep the frequency from 0.5 Hz to 5 MHz. It has four digits LED display. Fig. 26 shows BK Precision Function generator [48].


Fig. 26. BK Precision Frequency generator.

**CHILLER AND VACCUM PUMP**

In the present work we are using very high currents and oscillating magnetic field at frequencies above 100 kHz as stated above. These two factors generate heat and heat up the copper coil. This heating of the coil will increase further with increasing frequency. So in order to dissipate the generated heat, the coil has to be cooled externally. For this purpose water was injected into the set up due to its high heat capacity (4.187 $J/g^0C$) and it will take large amount of heat energy. The water chiller keeps the water that cools the coil externally at constant temperature. All the experiments were done at room temperature of 20°C. The chiller has a broad range of temperatures of the water it can operate on. Also, in order to prevent short circuiting from the ions of the water, copper sheets of the custom coil were isolated and distilled water was used [40]. The vacuum pump sustains a constant flow-rate in the pipes. But the water being pumped into the coil was not able to take all amount of the heat released by the coil. Hence, there will be some heat transfer to the sample by convection. So, vacuum pump [49] is connected to the coil enclosure to eliminate conduction and convection from the coil to the nanoparticle sample inside it and it pumps all the air out of the coil which in turn creates a vacuum inside the coil. This will stop any chance of heat transfer to the sample and raise in the temperature of the nanoparticle sample was solely due to increase in the temperature of the nanoparticles.

Fig. 27. Vacuum pump.

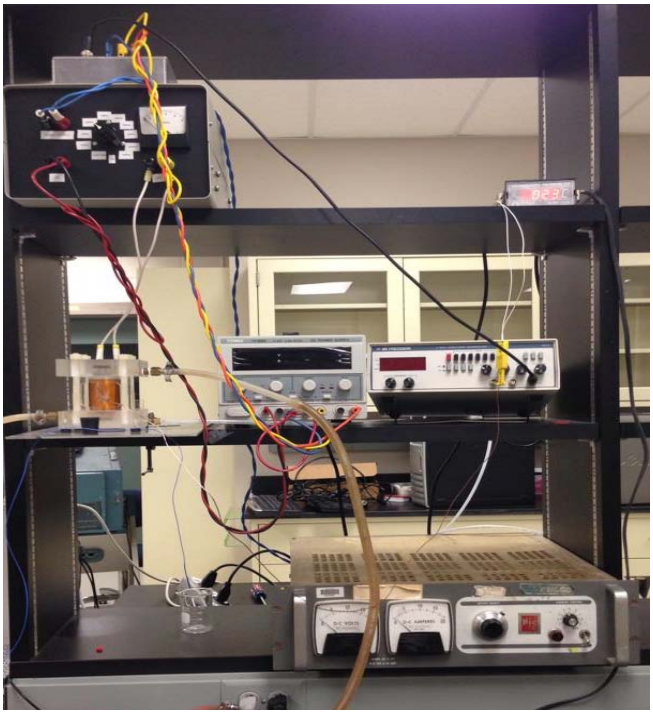

Fig. 28. Complete AMF system including custom-made power supply, frequency generator, current supply, and custom-made coil.

**SAMPLE CONTAINER**

The sample was taken in nuclear magnetic resonance (NMR) tubes with outer diameter of 5mm and small inner diameter of 4.57 mm with length of 7 inches. Fig. 29 shows a sample in NMR tube.

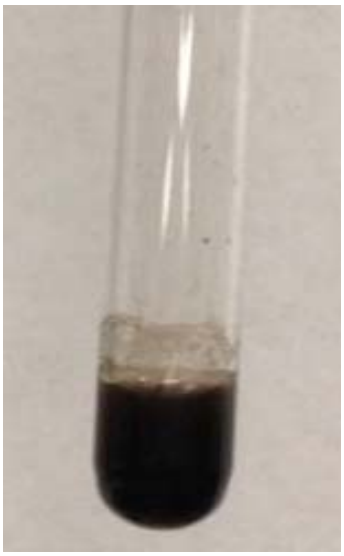

Fig. 29. NMR tube with a sample.

**MASS BALANCE**

A very precise mass balance was used to that can measure to the nearest tenth of thousand grams (0.0001 g). The mass balance was shielded on sides by glass plates to avoid any effects from surrounding conditions and was placed inside a lab hood (Fig. 30). Firstly, mass of each tube was measured alone and we used a weighing paper to transfer sample into the tubes. Then, the total mass of tube and a sample were measured together. We used the same amount of sample for measurements. Mass of nanoparticles was calculated by subtracting mass of tube from total mass of nanoparticle sample and tube together (see Table III). Measurements were done with a wet sample so 0.1 ml (0.1 g) of water was added to the sample. Water regular injection needle was used for adding water. It was ensured that no water resides on the wall of the tube.

Table III. Mass of sample and water.

| | |
|---|---|
| Mass of sample | 0.015 g |
| Mass of water | 0.1 g |

Fig. 30. Mass balance and injection needle.

**SONICATOR**

For evenly dispersing nanoparticles in water, a sonicator (Fig. 31) was used. It works on the principle of applying sound energy to agitate sample. The NMR tube containing nanoparticles and water was placed in a sonicator for about half hour or more (such that the sonicator completes 6-7 cycle) until nanoparticles are totally dispersed in water. The opening of the tube was sealed with para-film barrier film in order to avoid entrance of extra water from the sonicator into tube.


Fig. 31. A Sonicator.

**EXPERIMENTAL PROCEDURE**

A known amount of iron nanoparticle samples and water were put in NMR tubes and set to sonicate for half hour and after sonication, a fiber optics temperature probe was inserted inside the tube. To ensure proper position of the probe inside the tube all the time during the measurements, a duct

tape was wrapped around the temperature probe and opening of the tube. It eradicated any possibility of movement of temperature sensor. As mentioned before, the inner diameter of the NMR tubes are so small that a very small amount of sample is required to have a reasonable height of the sample and water. Also, the structure of the sensor has an influence on minimum amount of the sample needed to assure that the sensitive part of the sensor was imbedded in the sample. Tube containing wet sample along with temperature probe was placed in a black rubber holder. This was done to set the tube in the middle of the coil all the time. Firstly, water chiller and then vacuum pump was turned on. The above mentioned arrangement of tube containing wet sample was put inside the custom-made coil and waited for around 10 minutes in order to ensure that the vacuum inside the coil is stable also that the heat is no longer dissipated into the surroundings. Power supply and function generator was turned on and a frequency of 175 kHz was set in function generator. FISO Evolution software was opened and it was ensured that software is measuring temperature, else device was refreshed from the software. Recording time of the data logger was set to 15 minutes. Sample was then subjected to magnetic heating by turning on current supply to 15 A and sample was allowed to heat up for 4 minutes, then current supply was turned off. Sample was allowed to cool down for 11 minutes. Then whole system was turned off. After this tube containing sample and probe was taken out from the coil. The same experimental procedure was followed for 5 A and 10 A. Experiments with each sample was repeated for three different frequencies and three different current values. So, frequency was changed from 175 kHz to 130 kHz and finally to 88 kHz. Experiments were done for three different current values i.e., 5 A, 10 A, and 15 A for each frequency. All the data for temperature variation of nanoparticles was recorded by the FISO software. A typical sample plot is shown in Fig. 32 (BKFe25 at 15 A and 175 kHz). Nanoparticle

samples were dispersed in water by sonication to eradicate any sedimentation of the sample in water if it appears.

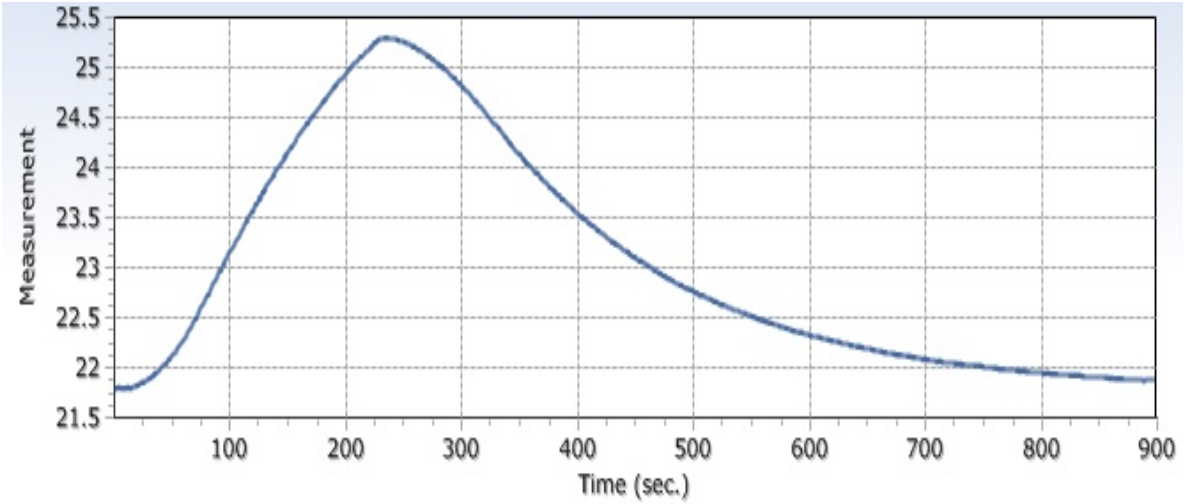


Fig. 32. Temperature variation of BKFe25 nanoparticles with time as sample is heated up and cooled down at 15 A and 175 kHz.

## IX. EXPERIMENTAL RESULTS

We are mainly interested in heating rate of the magnetic nanoparticles when irradiated by alternating magnetic field. The data of temperature changes with time recorded by FISO evolution software was loaded on MATLAB for further analysis. Our main focus will be to discuss only heating curves for all samples. The typical graph of temperature change (degree Celsius) versus time (seconds) is plotted in Fig. 33.

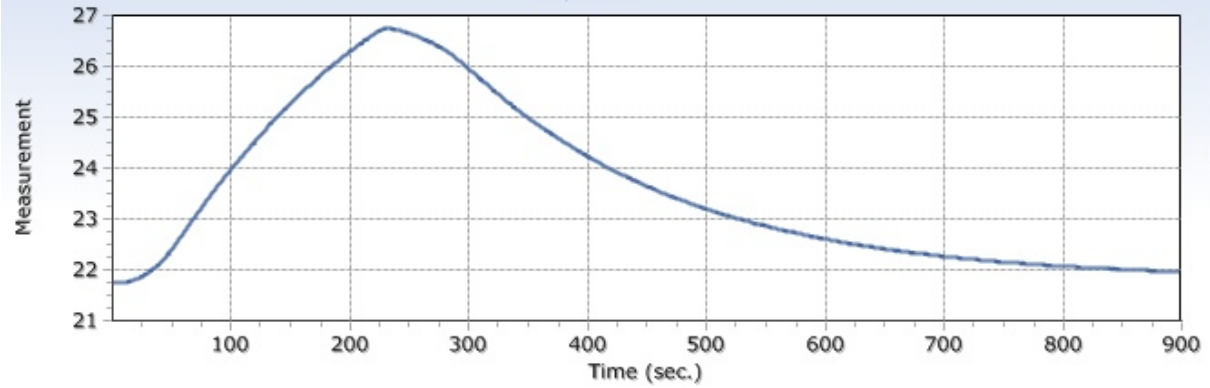


Fig. 33. Temperature variation of BKFe20 nanoparticles with time as sample is heated up and cooled down at 15 A and 130 kHz.

### HEATING RATE

The data obtained from the experiment, as an example, was plotted in Fig. 34 and since the heating rate is of interest to us, we have to find the change in temperature per unit time from the graph. It can be obtained by finding the initial (the highest) gradient of the heating curve. For this we choose to fit a third degree polynomial to the curve and inflection point was calculated by putting double derivative of the function to zero. Finally, the initial gradient (slope) of the heating rate was calculated at the inflection point. A best fit line (cubic approximation) is represented by following Eq. (74) where temperature is a function of time and a, b, c, d are the coefficients of the third degree polynomial.

$$T(t) = at^3 + bt^2 + ct + d \tag{74}$$

Second derivative of above equation is calculated and was set equal to zero to get inflection point $t_{INF}$. Finally, slope or heating rate was calculated at inflection point (see, Eq. (75))

$$Slope = dT/dt \text{ at } t = t_{INF} \tag{75}$$

Heating rates ($^0$C/sec) of different iron nanoparticle samples at different set of frequency and current are summarized in Tables IV-VI. Also, one typical plot with cubic approximation is shown in Fig. 34. The blue line corresponds to best fit curve and original data with error bars. These heating rates were used to find the specific power loss (SPL) or specific absorption rate (SAR) of iron nanoparticles.

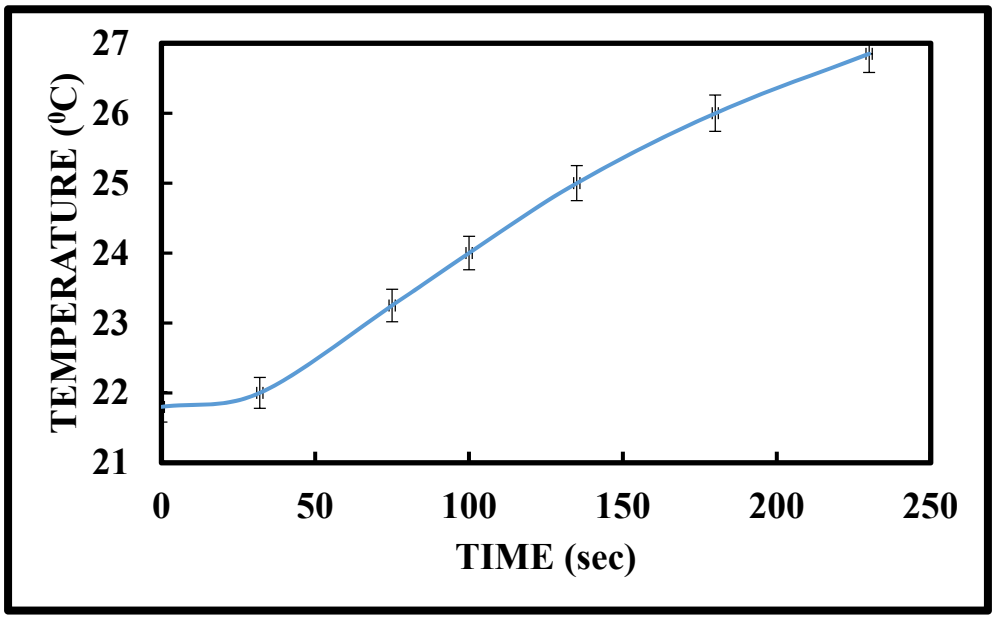


Fig. 34. Temperature variation of BKFe20 nanoparticles with time as sample is heated up at 15 A and 130 kHz following fitting curve with error bars.

**SPECIFIC POWER LOSS OR SPECIFIC ABSORPTION RATE (SAR)**

SPL or SAR is a measure of the heating ability of magnetic nanoparticles. SAR defines the power per unit mass of nanoparticles ([50]-[53]). By using the calorimetric formula, SAR can be defined as follows (Eq. (76))

$$SAR = C(\Delta T/\Delta t) \tag{76}$$

where C is the specific heat capacity of the nanoparticle sample which is calculated as mass weighed mean value of nanoparticles and water in units of J/g$^0$C and ($\Delta T/\Delta t$) is the initial slope of time-dependent temperature curve or heating curve in units of $^0$C/sec (Eq. (77))

$$C = \left(\frac{m_{np}c_{np}+m_w c_w}{m_{np}+m_w}\right) \tag{77}$$

where $m_{np}$ and $c_{np}$ and $m_w$ and $c_w$ are mass and specific heat capacity for nanoparticles and water (ignoring mass of container), respectively. In order to find the SAR for iron nanoparticles, we have to modify Eqs. (76)-(77) by dividing SAR (Eq. (76) by the mass fraction $m_{np}/(m_{np} + m_w)$ of iron nanoparticles and a new expression of the heat efficiency of iron nanoparticles ($SAR_{Fe}$) in units of Watt per gram (Eq.(78))

$$SAR_{Fe} = \left(\frac{m_{np}c_{np}+m_w c_w}{m_{np}}\right)\left(\frac{\Delta T}{\Delta t}\right) \tag{78}$$

Mass of iron nanoparticles and water used for SAR measurements and their respective heat capacities are summarized in Table VII. SAR (W/g) values for different iron nanoparticle samples are summarized in Tables VIII, IX, and X (percent error ≈ 6.7%).

Table IV. Heating rate of iron nanoparticles at 175 kHz for three current values of 5A, 10A, and 15A.

| Sample Name | Heating Rate at 175 kHz $\Delta T/\Delta t$ ($10^{-3}$ $^0$C/sec) | | |
|---|---|---|---|
| | 15 A | 10 A | 5 A |
| BKFe10 | 19.7 | 6.7 | 0.8 |
| BKFe15 | 5.1 | 1.8 | 0.4 |
| BKFe20 | 43.4 | 14.1 | 2.4 |
| BKFe25 | 21.3 | 6.0 | 1.1 |
| Fe9 | 9.3 | 3.2 | 0.8 |
| PTFe2 | 7.8 | 2.0 | 0.4 |
| PTFe3 | 14.5 | 5.6 | 0.9 |
| PTFe4 | 2.6 | 0.7 | 0.3 |
| PTFe5 | 1.0 | 0.8 | 0.4 |
| PTFe7 | 0.7 | 0.9 | 0.3 |

Table V. Heating rate of iron nanoparticles at 130 kHz for three current values of 5A, 10A, and 15A.

| Sample Name | Heating Rate at 130 kHz $\Delta T/\Delta t$ ($10^{-3}$ $^0$C/sec) | | |
|---|---|---|---|
| | 15 A | 10 A | 5 A |
| BkFe10 | 15.2 | 2.9 | 1.7 |
| BkFe15 | 2.0 | 0.9 | 0.2 |
| BkFe20 | 29.0 | 9.6 | 1.2 |
| BkFe25 | 14.0 | 3.2 | 0.6 |
| Fe9 | 5.4 | 1.3 | 0.6 |
| PTFe02 | 3.8 | 1.3 | 0.5 |
| PTFe03 | 12.1 | 2.6 | 0.5 |
| PTFe04 | 1.6 | 0.7 | 0.4 |
| PTFe05 | 1.4 | 0.5 | 0.1 |
| PTFe07 | 1.3 | 0.6 | 0.2 |

Table VI. Heating rate of iron nanoparticles at 88 kHz for three current values of 5A, 10A, and 15A.

| Sample Name | Heating Rate at 88 kHz $\Delta T/\Delta t$ ($10^{-3}$ $^0$C/Sec) | | |
|---|---|---|---|
| | 15 A | 10 A | 5 A |
| BKFe10 | 8.6 | 2.8 | 0.2 |
| BKFe15 | 1.1 | 0.6 | 0.1 |
| BKFe20 | 12.4 | 2.5 | 1.1 |
| BKFe25 | 6.6 | 1.8 | 0.4 |
| Fe9 | 4.6 | 1.5 | 0.2 |
| PTFe02 | 1.6 | 0.5 | 0.2 |
| PTFe03 | 5.5 | 1.4 | 0.3 |
| PTFe04 | 0.8 | 0.5 | 0.2 |
| PTFe05 | 1.0 | 0.4 | 0.2 |
| PTFe07 | 0.7 | 0.3 | 0.3 |

Table VII. Specific heat capacities and mass of Fe nanoparticles and water.

| Name | Heat capacity at 293K ($J/g^0C$) | Mass (g) |
|---|---|---|
| Water | 4.187 | 0.1 |
| Fe | 0.450 | 0.015 |

Table VIII. SAR values of iron nanoparticles at 175 kHz for three current values of 5 A, 10 A, and 15 A.

| Sample Name | SAR at 175 kHz ($10^{-1}$ W/g) | | |
|---|---|---|---|
| | 15 A | 10 A | 5 A |
| BKFe10 | 5.6 | 1.9 | 0.2 |
| BKFe15 | 1.5 | 0.5 | 0.1 |
| BKFe20 | 12 | 4.0 | 0.7 |
| BKFe25 | 6.0 | 1.7 | 0.3 |
| Fe9 | 2.6 | 0.9 | 0.2 |
| PTFe2 | 2.2 | 0.6 | 0.1 |
| PTFe3 | 4.1 | 1.6 | 0.3 |
| PTFe4 | 0.7 | 0.2 | 0.1 |
| PTFe5 | 2.9 | 0.2 | 0.1 |
| PTFe7 | 0.2 | 0.2 | 0.1 |

Table IX. SAR values of iron nanoparticles at 130 kHz for three current values of 5 A, 10 A, and 15 A.

| Sample Name | SAR at 130 kHz ($10^{-1}$ W/g) | | |
|---|---|---|---|
| | 15 A | 10 A | 5 A |
| BKFe10 | 4.3 | 0.8 | 0.5 |
| BKFe15 | 0.6 | 0.2 | 0.07 |
| BKFe20 | 8.2 | 2.7 | 0.3 |
| BKFe25 | 3.9 | 0.9 | 0.2 |
| Fe9 | 1.5 | 0.4 | 0.2 |
| PTFe2 | 1.1 | 0.4 | 0.1 |
| PTFe3 | 3.4 | 0.8 | 0.1 |
| PTFe4 | 0.5 | 0.2 | 0.1 |
| PTFe5 | 0.4 | 0.1 | 0.3 |
| PTFe7 | 0.4 | 0.2 | .004 |

Table X. SAR values of iron nanoparticles at 88 kHz for three current values of 5 A, 10 A, and 15 A.

| Sample Name | SAR at 88 kHz ($10^{-1}$ W/g) | | |
|---|---|---|---|
| | 15 A | 10 A | 5 A |
| BKFe10 | 2.4 | 0.8 | 0.002 |
| BKFe15 | 0.3 | 0.2 | 0.03 |
| BKFe20 | 3.5 | 0.7 | 0.03 |
| BKFe25 | 1.9 | 0.5 | 0.01 |
| Fe9 | 1.3 | 0.4 | 0.01 |
| PTFe2 | 0.5 | 0.2 | 0.05 |
| PTFe3 | 1.5 | 0.4 | 0.07 |
| PTFe4 | 0.2 | 0.1 | 0.02 |
| PTFe5 | 0.3 | 0.1 | 0.05 |
| PTFe7 | 0.2 | 0.1 | 0.04 |

# X. DISCUSSION

After the experiments and experiment results (heating rates and SAR values) for different iron nanoparticles were obtained, we have enough data to proceed with the analysis. In this chapter will elaborate how particle size effects heating rates and SAR values. We will find out the critical particle size of different iron nanoparticles for single-domain to multi-domain transition ($D_{C1}$ for diameter and $R_{C1}$ for radius from now on) and single-domain to superparamagnetic transition ($D_{C2}$ for diameter and $R_{C2}$ for radius from now on) with the help of SAR and the relationship between frequency, current and particle size will also be obtained. Finally, surface effects on the critical particle size will also be analyzed.

## EFFECT OF DIFFERENT PROPERTIES ON HEATING RATE OF NANOPARTICLES

As discussed in Chapter VI, the heating effects of single-domain, multi-domain and superparamagnetic nanoparticles subjected to alternating magnetic fields are due to several type of loss mechanisms and contributions of each will depend strongly on particle size and other properties like applied frequency and current.

## EFFECT OF NANOPARTICLE DIAMETER ON SAR

A graph between SAR values for different sample size of iron nanoparticles was drawn in Fig. 35. The frequency was altered from 88 kHz to 175 kHz for the highest current value of 15A used in our experiment. We took average of particle size summarized in Table I.

When SAR is plotted against average particle diameter in Fig. 35, we observe two maxima of heating efficiency due to size-dependent hysteresis and relaxation behavior, which become more pronounced as the frequency increases from 88 kHz to 175 kHz. One of the peaks occurs at 8 nm and another at 18 nm representing maxima value of SAR, respectively. First maximum at 8 nm belongs to superparamagnetic regime of iron nanoparticles. This maximum represents crossover

between Neel and Brownian heating mechanisms resulting in maximum value of heat in superparamagnetic regime. The transition from single-domain to superparamagnetic behavior occurs at a critical size of 10 nm i.e., $D_{C2}$ = 10 nm. Second maximum at 18 nm i.e., $D_{C1}$ = 18 nm corresponds to the critical size of iron nanoparticles when transition from single-domain to multi-domain regime occurs. Referring back to Chapter III, the plot (Fig. 9), between coercive field and nanoparticles diameter showing transition from single to multi-domain regimes, directly supports the critical sizes, we get from SAR vs mean diameter (Fig. 35). Thus, coercive field and SAR shows similar dependence on nanoparticles diameter.

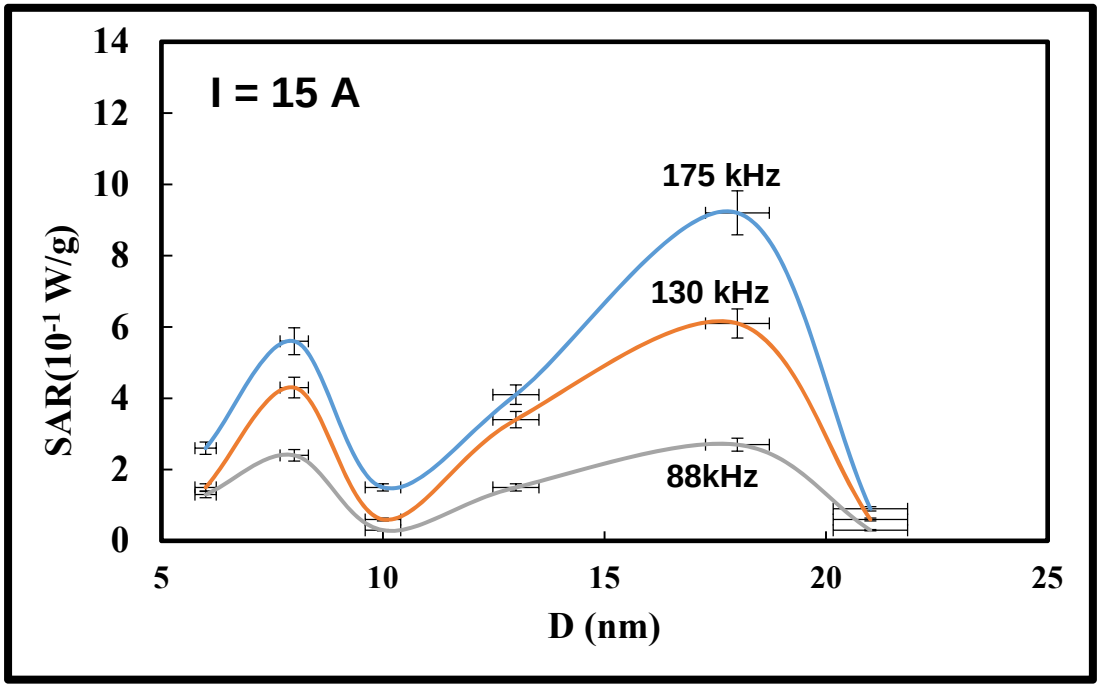


Fig. 35. The effect of nanoparticle size on SAR at 15 A for three different frequencies: 88 kHz, 130 kHz, and 175 kHz.

The heat efficiency for single-domain, multi-domain and superparamagnetic nanoparticles is due to hysteresis loss and Neel-Brown relaxation losses. As discussed in Chapter VI, Neel relaxation process is the major determinant in the peak for heating curve at small diameter of nanoparticles. At the same time, Brownian relaxation process is also prominent as suspending medium used in

the present case is water, which has low viscosity of 0.0009 kg/m•sec. As a result, nanoparticles can align themselves with switching external field, which in turn will increase the overall SAR. It can be seen from Fig. 35 that SAR increases as nanoparticle size increases and is higher for nanoparticle size around 8 nm and decreases further as size increases. For further increase in nanoparticle size SAR increases and reaches the highest value for nanoparticle size around 18 nm and further decreases as particle size increases. It can also be seen from Fig. 35 that for lower frequency of 88 kHz, SAR is not prominent but as frequency increase to 175 kHz, there is good increase in SAR values for 15 A of current. Referring back to the equation of volumetric power generation P in Chap.VI, power depends directly on the applied frequency and square of the applied field strength. We can say that applied frequency and applied field strength is a major contributor of the total power generated by ferromagnetic nanoparticle system.

From Fig. 35, we can conclude that particle size and applied frequency played a crucial role in magnitude of value of specific absorption rate. Higher frequency results in high heat efficiency. The similar relationship is observed when SAR is plotted against particle diameters for different current values of 5 A, 10 A and 15A at the highest applied frequency of 175 kHz in Fig. 36. We observe two maxima of heat efficiency due to size-dependent hysteresis and relaxation losses. SAR is higher for high currents (blue color curve in Fig. 36) and low for low current (gray curve in Fig. 36). We can conclude that high current strength results in high heat efficiency.

**EFFECT OF CURRENT ON SAR**

If SAR is plotted against current at two diameters of 8 nm and 18 nm with 175 kHz of applied frequency, we observe a strong dependence of SAR on current or intensity of applied field (Fig.37).

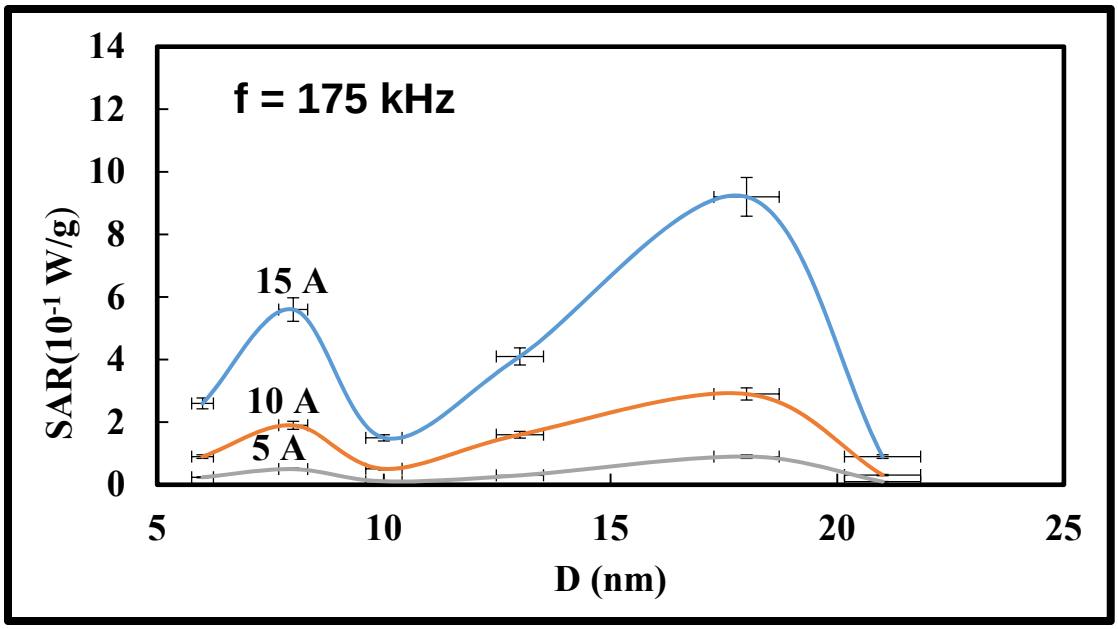


Fig. 36. The effect of nanoparticle size on SAR at 175 kHz for three different currents: 5 A, 10 A, and 15 A.

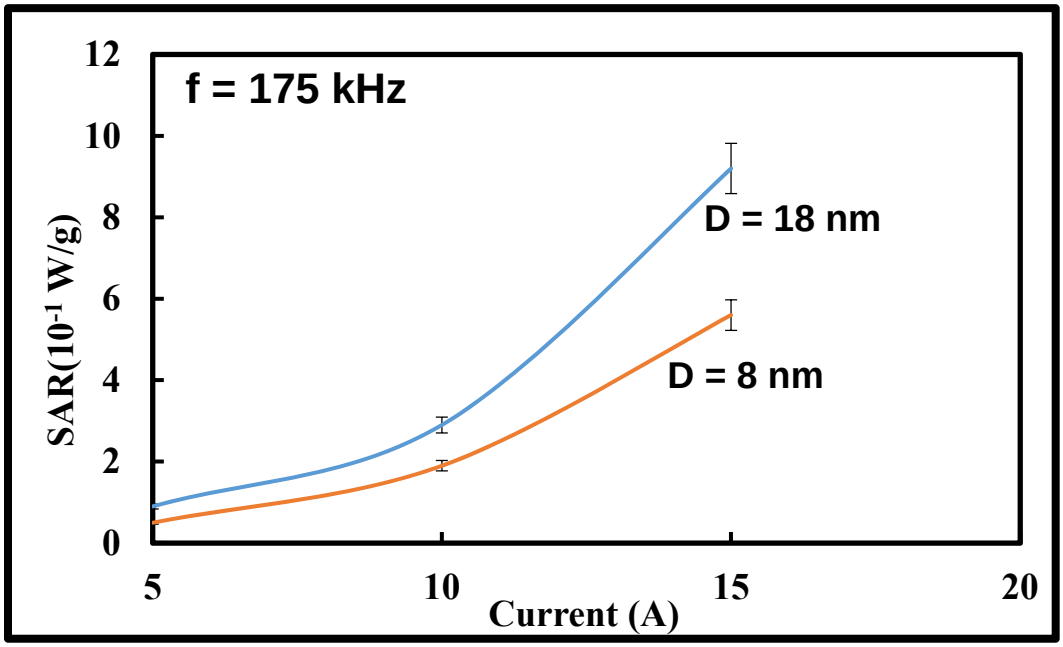


Fig. 37. The effect of current on SAR of iron nanoparticles for 8 nm and 18 nm in diameter at 175 kHz.

We can conclude from Fig. 37, that higher current intensity produces higher SAR value but this relationship further depends on nanoparticle size, as for larger diameter (18 nm) SAR is higher in

comparison to 8 nm nanoparticle size, for which SAR has lower values. This result is important and similar relationship between current and SAR was also observed in [31] as can be seen from Fig. 38.

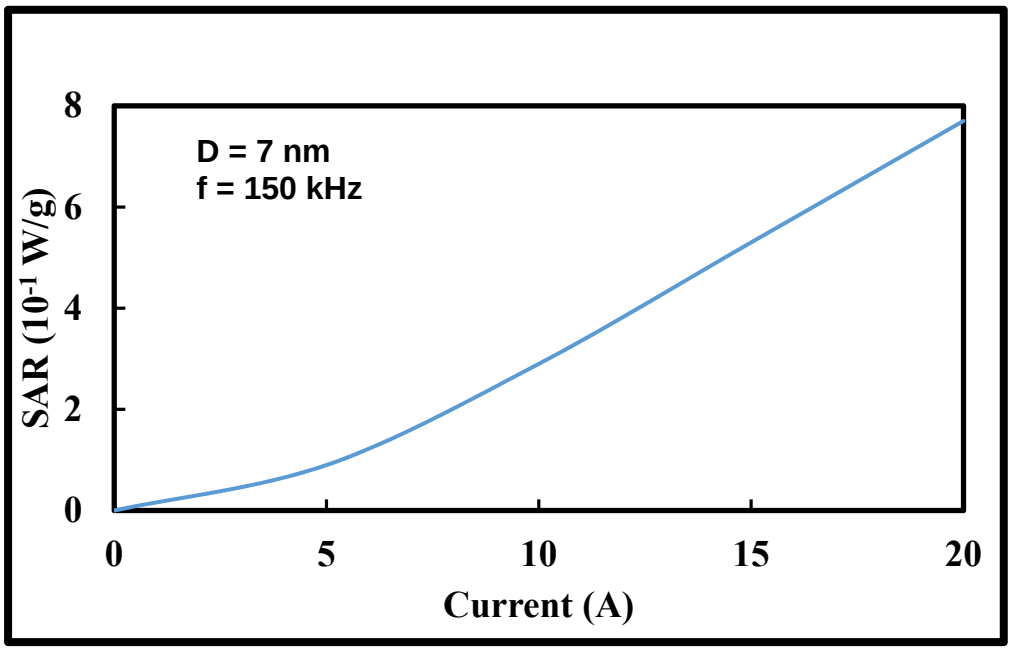


Fig.38. The dependence of SAR on current (applied magnetic field) for ferromagnetic nanoparticles with D = 7 nm [31].

**EFFECT OF APPLIED FIELD FREQUENCY ON SAR**

If SAR is plotted against applied frequency at two diameters of 8 nm and 18 nm with 15A current, we observe a strong dependence of SAR on applied frequency (Fig. 39). We can conclude that higher frequency produces higher SAR value but this relationship further depends on particle size, as for larger diameter (18 nm) SAR is higher as comparison to 8 nm nanoparticle size, for which SAR has lower values. This is a very important result since SAR has a proportional relationship with the frequency of the applied magnetic field and this also verifies the equation which was derived in Chapter VI. Similar linear relationship between applied frequency and SAR was also observed in [31] as can be seen from Fig. 40.

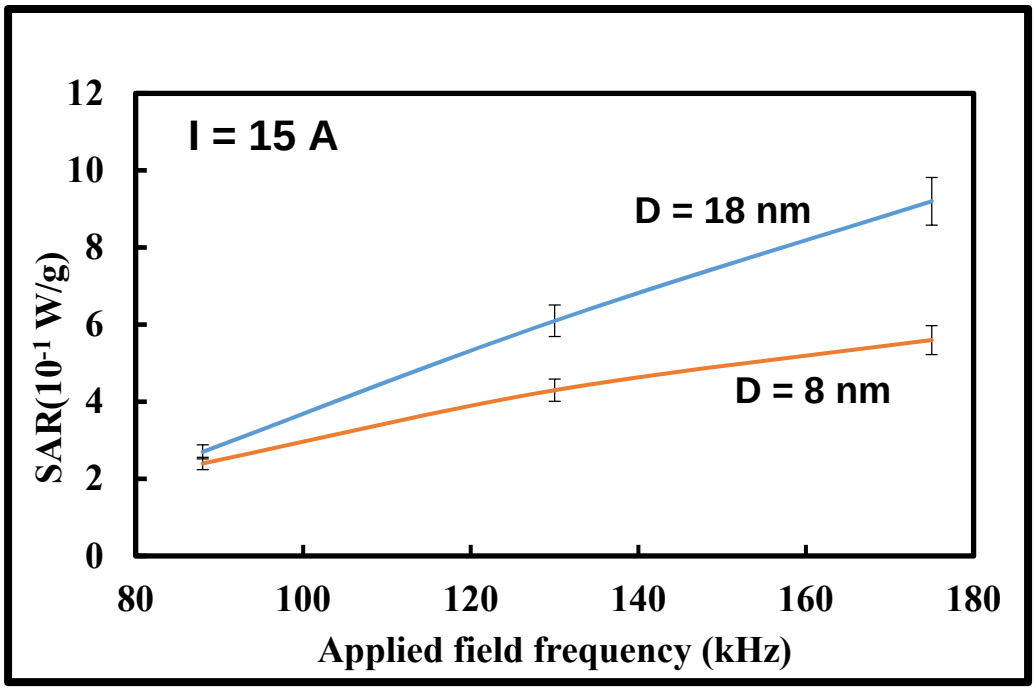


Fig. 39. The effect of frequency on SAR of iron nanoparticles for 8 nm and 18 nm in diameter at 15 A.

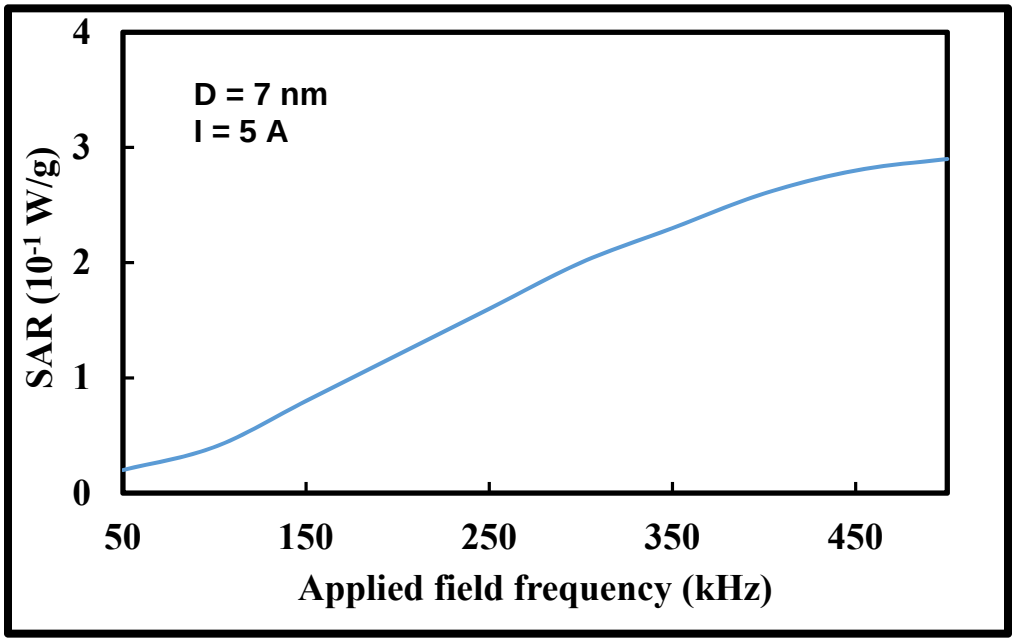


Fig. 40. The dependence of SAR on frequency [31].

**LOW-ANISOTROPY SURFACE EFFECTS ON CRITICAL NANOPARTICLE SIZES**

The critical size of nanoparticles for low anisotropy case was already discussed in Chapter V.

The equation describing the critical size of magnetic nanoparticles is given below (see, Eq. (79))

$$\left(\frac{8\pi^2}{9}\right) {M_s}^2 R^3 = (2\pi JR/a)[ln\left(\frac{2R}{a}\right) - 1] \tag{79}$$

In Eq. (79), we are introducing surface effects in terms of fitting parameters α and β lead us to the new Eq. (82) in terms of critical radius. $M_S$ is replaced by Eq. (80) and J is replaced by Eq. (81).

$$M_S(R) = M_{S0}\left(1 - \frac{\alpha}{R}\right) \tag{80}$$

$$J(R) = J_0\left(1 - \frac{\beta}{R}\right) \tag{81}$$

$$\left(\frac{8\pi^2}{9}\right)\left(M_{S0}\left(1 - \frac{\alpha}{R}\right)\right)^2 R^3 = J_0\left(1 - \frac{\beta}{R}\right)(2\pi R/a)\left[\, ln\left(\frac{2R}{a}\right) - 1\right] \tag{82}$$

In C++ program, the following replacements were done. Fig. 41 and Fig. 42 show effects of surface parameters α and β on critical radius.

With a = A and R = X, Eq. (82) modifies into the following Eq. (83)

$$\left(\frac{8\pi^2}{9}\right)\left(M_0\left(1 - \frac{\alpha}{X}\right)\right)^2 X^3 = J_0\left(1 - \frac{\beta}{X}\right)(2\pi X/A)\left[\ln\left(\frac{2X}{A}\right) - 1\right] \tag{83}$$

Also, for more advancement, Eq. (83) was solved further with replacements in terms of following Eq. (84) and Eq. (85)

$$\left(1 - \frac{\alpha}{R}\right) = 4\left\{1 - \frac{1}{(4R/_{ch})-1}\right\} \times exp\left\{-\frac{2S_b}{3R_g}\frac{1}{(4R/_{ch})-1}\right\} - 3 \tag{84}$$

$$\left(1 - \frac{\beta}{R}\right) = \left\{1 - \frac{1}{(4R/_{ch})-1}\right\} exp\left(-\frac{2S_b}{3R_g}\frac{1}{(4R/_{ch})-1}\right) \tag{85}$$

When c, h and $S_b$ are fixed and α increases with increasing size and approaches a limited value $\alpha_{max}$. On the other hand β decreases with increase in particle size. The constant c

$(0 < c \leq 1)$ shows the normalized surface area given by c = 1 for low-dimensional materials with free surface and has higher values for high-dimensional materials $(1 < c \leq 2)$ [25].

This program is summarized as follows [54]:

```
#include <iostream>
#include <stdlib.h>
#include <fstream>
#include <math.h>

// J0/A taken from Kittel
#define J0_A  2.0
#define A 0.35
//2pi*MS2 /3=6.0e-15
#define M02 6.0e-2
#define M_PI       3.14159265358979323846
// constant [J/mol K]
#define R 8.314466
// constant h[nm]
#define H 0.2482
// constant Sb[J/mol K]// Big number
#define SB 110.7
using namespace std;
long double fun(long double, long double, long double);
void main()
{
        long double x,a,b,a1,b1,err=1.0,eps=1.0e-7;
         long double ia,jb; //alfa,beta
         int i,j;
         ofstream results("results_svib.txt");
         ofstream resultsfun("wart_fun.txt"); // checks if RC is a solution
         cout<<"  give a=";
         cin>>a1;
         cout<<" \n give b=";
         cin>>b1;
         //bool la=true;
         cout<<" b-a="<<(b1-a1)<<endl;
         for(i=0;i<100;i++) ///for(i=0;i<50;i++)
         {
                 ia=0.1*i + 2;            //ia=0.1*i;
                 Results<<ia<<" ";
                 for(j=1;j<5;j++)    ///for(j=0;j<50;j++)
                 {
                          a=a1; b=b1;
                          jb=0.01*j;                        //jb=0.01*j;
                         int numerator=0;
```

```
                        //long double y,z,xx;//x+(b-a)
                        x=a;
                        while(fun(a,ia,jb)*fun(b,ia,jb)>0 && numerator<10000)
                        {   a=x+(b-a)*((double)rand())/RAND_MAX;
                    //cout<<a;
                        numerator++;
                        }
                        if(numerator==10000)
                        {
                                results<<"-0 ";
                                cout<<"-0 ;";
                        }
                        else
                        {
                                while ((b-a)>eps)
                                {
                                        x=(b+a)/2;
                                        if(fun(a,ia,jb)*fun(x,ia,jb)>0) a=x; else b=x;
                                }
                 cout<<numerator;
                                x=(b+a)/2;
                                results<<x<<" ";
                                resultsfun<<fun(x,ia,jb)<<" ";
                                cout<<"x="<<x<<"\n";
                        }
                }
                results<<endl;
                resultsfun<<endl;
        }
}
/*long double fun(long double x,long double alfa,long double beta)
{
        long double result=0;
        result=4*x*x*M0^2*(1-alfa/x)*(1-alfa/x)/3-J0_A*(1-beta/x)*(log(2*x/A)-1);
        return result;
}*/
long double fun(long double x,long double Svib,long double c)
{
        long double result=0,zz;
        zz=4*(1-1/(2*x/(c*H)-1))*exp(-(2/3)*(SB/(2*R/(c*H)-1)))-3;
        result=4*x*x*M0^2*zz*zz/3-J0_A*exp(-(2*Svib/(3*R))/(x/(6*H)-1))*(log(2*x/A)-1);
        return result;
}
long double fun1(long double x,long double parameter)
{
        long double result=0;
```

```
        result=x*x-4;
        return result;
}
```

From Fig. 41, we can see that critical radius $R_C = R_{C1}$ for the transition from single-domain to multi-domain configuration for low anisotropy is increasing with increase in surface parameter α in accordance with assumptions made in Chapter V. According to which, by increasing thickness of surface layer α (increase in number of surface atoms of the nanoparticles having disordered magnetic moments), the saturation magnetization is diminished.

Also, it can be seen from Fig. 42, that critical radius for transition from single-domain to multi-domain configuration of iron nanoparticle decreases with increasing value of surface parameter β affecting Curie temperature and exchange integral.

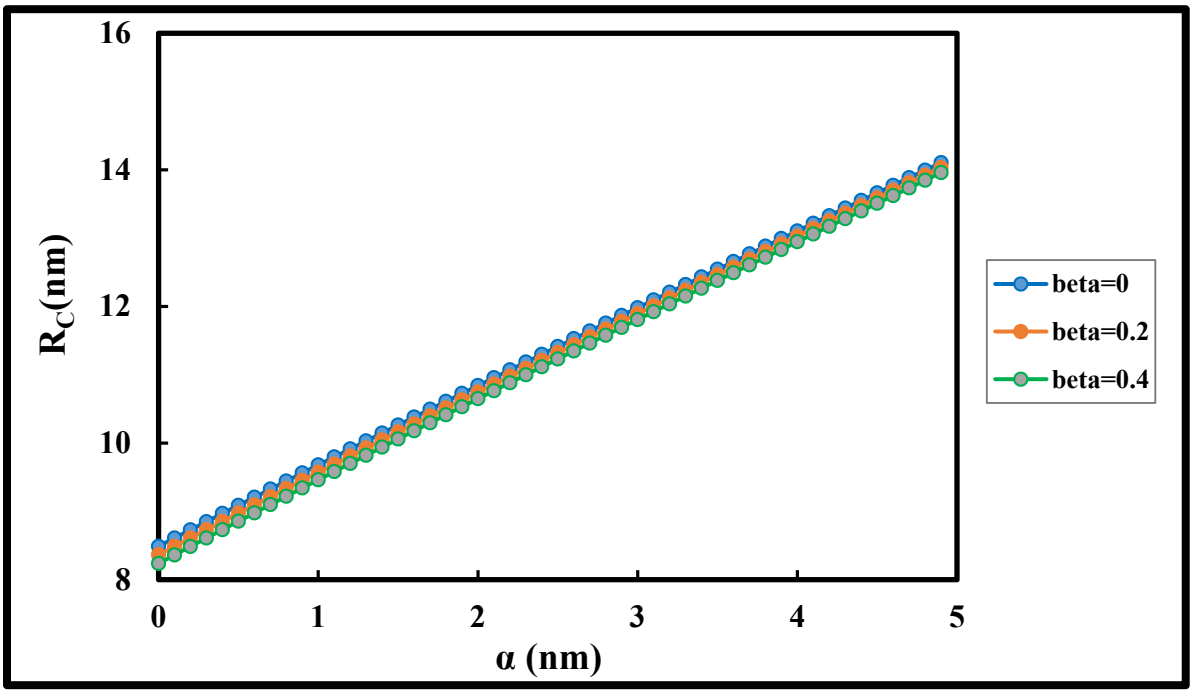


Fig. 41. The effect of surface on critical size of iron nanoparticles when parameter β is kept constant.

Again, this result is in accordance with the assumptions made in Chapter V that, reducing the size of nanoparticle leads to decrease in exchange interactions between atoms on the surface of the nanoparticles, which in turn leads to the suppression of Curie temperature of nanoparticle. It is clear from Fig. 41 and 42, that surface effects has significant influence on the critical size of nanoparticles.

In Table XI, available experimental values of critical diameters of iron and iron related nanoparticles for the transition from single-domain to multi-domain, $D_{C1}$ and from single-domain to superparamagnetic regime, $D_{C2}$ are given. There is considerable distribution of critical diameters values for iron nanoparticles from 8 nm to 20 nm for single-domain to superparamagnetic transition and from 5 nm to 40 nm for single-domain to multi-domain transition due to possibly surface effects. Large differences in critical size values could be also due to the fabrication methods of magnetic nanoparticles as well due to their shapes.

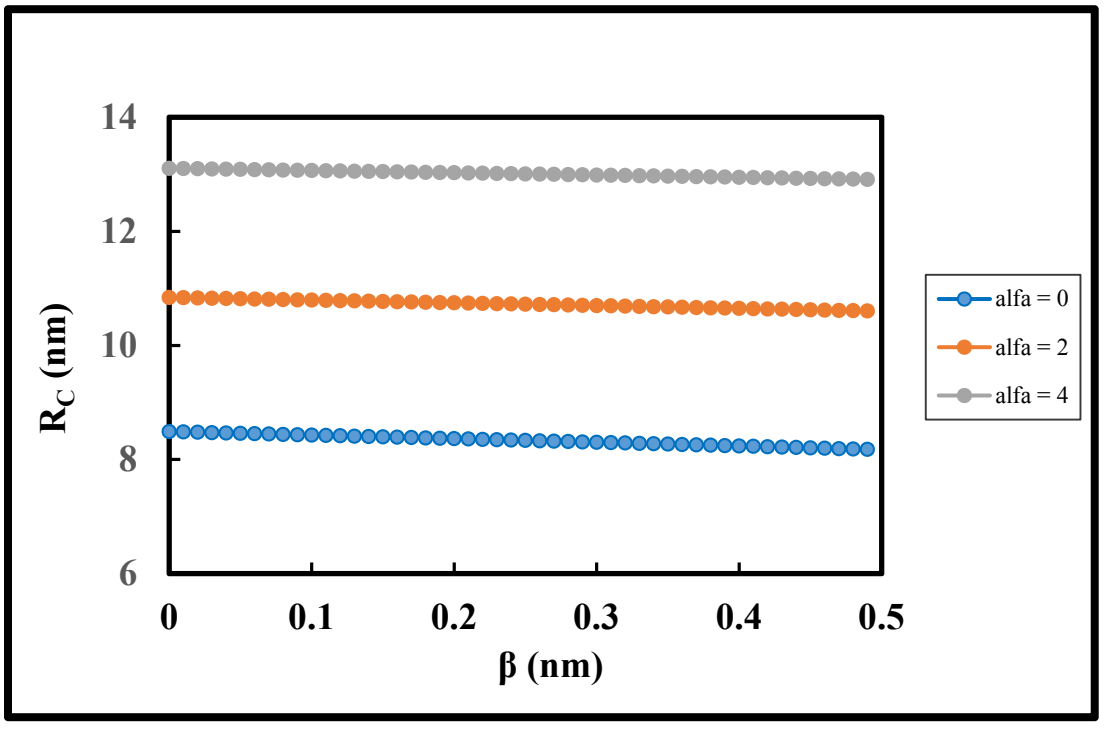


Fig. 42. The effect of surface on critical size of iron nanoparticles when α is kept constant.

Let us now try to estimate the critical size of iron nanoparticles by incorporating BOLS correlation model into our experimental result (Figs. 35–36) and connect it with surface effects (Fig. 41– 42) for weak anisotropy. In terms of BOLS correlation at room temperature, parameters α and β related to surface thicknesses are described by Eqs. (52), (54) in terms of known parameters c, h and $S_b$. For iron c = 1, h = 0.2482 nm [25], $S_b$ = 110.7 J $g^{-1}$ atom $^{-1}$ $K^{-1}$ [25], and Rg = 8.3144 J $K^{-1}$ $mol^{-1}$ [61]. Plugging these values to Eq. (52) and (54) the α and β are:

$$\alpha \approx ch(2 + \frac{4S_b}{3R_g}) \approx 4.9 \text{ nm and } \delta \approx \alpha/4 \approx 1.2 \text{ nm.}$$

Here δ has the same value as β in accordance with Eqs. (57), (58). From Fig. 41 for α ≈ 4.9 nm, the value of critical radius of iron nanoparticle for transition from single-domain to multi-domain is approximately $R_{C1}$ = 14 nm (for β ≈ 1.2 nm). These two results are perfectly matching with each other. Hence, by incorporating BOLS correlation theory into experimental results, values for critical radius reconciles very well. Moreover, from experimental results on SAR of iron nanoparticles, the value of $R_{C1}$ was found to be around 9 nm ($D_{C1}$ =18 nm) from Figs. 35–36. This value of $R_{C1}$ occurs for smaller value of α ≈ 1 nm and β ≈ 0.1 nm as it can be seen from Figs. 41–42. This result is further evidence of the tremendous impact of surface layer on the critical size of nanoparticles due to atomic coordination number imperfection of the surface layer.

Table XI. Critical sizes $D_{C1}$ (transition from single-domain to multi-domain) and $D_{C2}$ (transition from single-domain to superparamagnetic phase) for iron and iron related nanoparticles.

| Materials | $D_{C1}$(nm) | $D_{C2}$(nm) | Reference |
|---|---|---|---|
| Fe | | 10 | [55] |
| Fe | 17-26 | 20 | [38] |
| Fe | 15 | | [4] |
| Fe | 5-25 | | [56] |
| Fe | | 16 | [15] |
| Fe | 25 | | [57] |
| $\gamma - Fe_2O_3$ | 26-53 | | [36] |
| $\gamma - Fe_2O_3$ | 91 | | [58] |
| $\gamma - Fe_2O_3$ | | 35 | [59] |
| $\gamma - Fe_2O_3$ | | 10 | [52] |
| $Fe_2O_3$ | 90 | 33 | [16] |
| $Fe_3O_4$ | 25 | | [53] |
| Pure $Fe_3O_4$ | | 16.5 | [33] |
| $Fe_3O_4$(oleic acid coating) | | 7.83 | [33] |
| $Fe_3O_4$ | 128 | 25-30 | [4] |
| $Fe_3O_4$ | 85 | 25 | [16] |
| $Fe_3O_4$ | 19-52 | | [36] |
| $Fe_3O_4$ | 83 | | [57] |
| $Fe_3O_4$ | | 21 | [58] |
| $Fe_3O_4$ | 30-40 | | [60] |
| bcc Fe | 8.3-15 | 8-20 | [36] |
| fcc Fe | 40 | | [36] |
| $MnFe_2O_4$ | 50 | | [53] |
| $CoFe_2O_4$ | 14 | | [53] |
| $Fe_{80}Si_{20}$ | 35 | | [57] |
| FeCo | 51 | 15-20 | [58] |
| FeCo | | 24 | [59] |
| FeCo | 51 | 15 | [16] |
| FePt | 53 | 5 | [16] |
| fcc FePt | 55 | | [58] |
| fcc FePt | | 10 | [59] |
| $CoFe_2O_4$ | 100 | 10 | [16] |

# XI. CONCLUSION AND FUTURE GOALS

As the introduction to this Thesis, we discussed basic concept of magnetism and different type of magnetic materials. Magnetism on atomic level arises from unpaired electrons spins, which behaves like atomic dipole moments. Different type of magnetism can be described by the material's response to an applied magnetic field. Out of all type of magnetism, ferromagnetism is the strongest form of magnetism which is due to strong exchange interactions between atomic moments. Ferrimagnetism is similar to ferromagnetism, but results from exchange interactions in ionic solids (mostly metallic solids like iron oxide). Both ferromagnetic and ferrimagnetic materials demonstrate strong enough internal interactions to maintain magnetization in the absence of an applied field but when a strong external magnetic field is applied, the atomic moments will align to the direction of externally applied field. Diamagnetism, paramagnetism, and antiferromagnetism normally demonstrate weak interactions. Following that, nanomagnetism and superparamagnetism was discussed. If the size of magnetic nanoparticles is maintained below a critical dimension, they tend to develop as single magnetic domain structures, and at the smallest sizes, they exhibit superparamagnetic behavior under standard conditions. Single-domain to multi-domain critical size corresponds to the point where it is energetically favorable for the magnetic nanoparticle to exist without a domain wall. As critical size of nanoparticles was of interest to us, the process of domain formation was discussed as the background for derivation of critical size equation of nanoparticles. Surface effect was the next issue to be addressed after the foundations of this Thesis have been laid. Surface effects on saturation magnetization, Curie temperature, anisotropy and exchange interaction were discussed. When solid size is reduced to nanometer scale, the magnetic properties are changed. At low temperature, the saturation magnetization increases inversely with size due to the contribution from the localized charges whereas at high

temperatures, saturation magnetization drops as the size is reduced because of the bond-order loss that is also responsible for suppression of Curie temperature. Effective anisotropy also increased due to surface effects. Here surface anisotropy is important, which is caused by the breaking of the symmetry and reduction of the nearest neighbor coordination on the surface layer. A foundation for the modification of critical size equation in terms of surface parameters have been laid, which has been solved numerically by using a program in C++.

Magnetic heating was the next issue to be addressed. The heating associated with ferromagnetism was quantified by hysteresis loss equivalent to area enclosed by hysteresis curve related to the power loss. Neel and Brown relaxation mechanisms and appropriate power losses were responsible for magnetic heating mostly in superparamagnetic nanoparticles subjected to ac magnetic field at low and high frequencies regimes. There is also frictional losses when nanoparticles are submerged in viscous fluid which results in additional heating.

Iron nanoparticles used in this research were prepared by thermal decomposition of iron precursor method in Cambridge University, United Kingdom with different mean diameters from 5.9 nm to 21.4 nm. Heating performance of these nanoparticles was measured experimentally using a calorimetric method. The same amounts of iron nanoparticles mixed with de-ionized water were irradiated by an alternating magnetic field and they liberate heat to their surrounding tissue which is water in present case. This heating performance of nanoparticles was described in terms of Specific Power Loss or Specific Absorption Rate (SAR) which depends on heating rate. Relevant equation for SAR was derived. Heating rate was calculated from the initial slope of temperature vs time. SAR was plotted against average nanoparticle diameter and we observed two clear peaks of heating efficiency due to size-dependent hysteresis and relaxation behavior. One of the peak at 8 nm and another at 18 nm represents maximum values of SAR. First peak at 8 nm belongs to

superparamagnetic regime of iron nanoparticles where contribution from Brown and Neel mechanism is optimized. The transition from single-domain to superparamagnetic behavior occurs at a critical size of 10 nm ($D_{C2}$). Second peak at 18 nm ($D_{C1}$) corresponds to the critical size of iron nanoparticles when transition from single-domain to multi-domain regime occurs and a maximum of coercive force is observed. SAR was also plotted against applied frequency and current which has a linear relationships. We found that the higher the value of current and frequency, the higher is SAR.

Towards the end of this Thesis, low anisotropy surface effects on critical size of iron nanoparticles were studied. For this study, equation for the critical radius for transition from single-domain to multi-domain was modified in terms of surface parameters and was solved numerically by using program written in C++ and graphs between critical radius and surface parameters $\alpha$ and $\beta$ were plotted. We found that single-domain to multi–domain critical size of nanoparticles increases with increasing $\alpha$, while slightly decreases with increasing $\beta$. Further, adequacy and reality of BOLS correlation theory was also proved and a critical diameter of 28 nm for the transition from single-domain to multi-domain regime was found which was different from the critical diameter of 18 nm found from SAR results, which further proved impact of surface layer on critical size. At the same time, critical sizes of different iron nanoparticles from various papers were also compared, differences in critical sizes further proved the tremendous impact of surface layer on the critical size of nanoparticles. We have noted that SAR value increases with nanoparticle size. However, as future prospects, effect of shape, composition and concentration of nanoparticle on SAR has to be established. In this research, we have studied the strong dependence of low anisotropy nanoparticle single-domain to multi-domain critical radius on its surface properties due to modification of Curie temperature, exchange integral constant and saturation magnetization.

Further studies are required to find the critical size of nanoparticle for high anisotropy and effect of anisotropy on the critical size has to be studied. Surface effects on coercivity, blocking temperature can also be considered. Along with the nanoparticle size, its shape also has an impact on the magnetic properties and not much research on shape aspect of nanoparticle has been conducted yet. So, impact of nanoparticle shape on the magnetic properties can be studied in future, which will provide a powerful tool for modifying the properties to enhance the effectiveness of magnetic nanoparticle in particular application.

## XII. REFERENCES


[1] A.E. Berkowitz, W.J. Schuele, and P.J. Flanders, J.Appl.Phys., 39 (1968) 1261.

[2] A. Marinin, "Synthesis and Characterization of Superparamagnetic Iron Oxide Nanoparticles Coated with Silica", Master Thesis, Stockholm, 2012.

[3] L.L.Vatta, R.D. Sanderson, and K.R. Koch, "Magnetic Nanoparticles: Properties and Potential Applications", Pure Appl. Chem., 78 (2006) 1793.

[4] A.H. Lu, E.L. Salabas, and F. Schuth, "Magnetic Nanoparticles: Synthesis, Protection, Functionalization, and Application", Angew.Chem.Int.Ed., 46 (2007) 1222.

[5] P. Curie, "On the Possible Existence of Magnetic conductivity and Free Magnetism", French Society of Physics, 76 (1894).

[6] http://en.wikipedia.org/wiki/Magnetic_monopole (online link for magnetic monopoles).

[7] P. Dirac. "Quantized Singularities in the Electromagnetic Field", Proc. Roy. Soc., 133 (1931) 60.

[8] http://en.wikipedia.org/wiki/Magnetization (online link for magnetization).

[9] F. T. Ulaby, "Fundamentals of Applied Electromagnetics", Pearson Education, Upper Saddle River, New Jersey, 2004.

[10] J. Yamauchi, "Fundamentals of Magnetism", Wiley-VCH Verlag Gmbh & Co., 2008.

[11] M. Getzlaff, "Fundamentals of Magnetism", Springer-Verlag Berlin Heidelberg, 2008.

[12] http://cnx.org/content/m22749/latest/ (online link for images).

[13] R.C. O' Handley, "Modern Magnetic Materials: Principles and Applications", Wiley, New York, 2000.

[14] http://en.wikipedia.org/wiki/Antiferromagnetism.

[15] http://en.wikipedia.org/wiki/Ferrimagnetism.

[16] A.G. Kolhatkar, A.C. Jamison, D. Litvinov, R.C. Wilson and T.R. Lee, "Tuning the Magnetic Properties of Nanoparticles", International Journal of Molecular Sciences, 14 (2013) 15977.

[17] A. Ghoshal, S. O. Raja, N. R. Bandyopadhyay, A. K. Dasgupta, "Superparamagnetic Iron Oxide Nanoparticle Attachment on Array of Micro Test Tubes and Microbeakers Formed on p-type Silicon Substrate for Biosensor Applications", Ray M - Nanoscale Res. Lett., 6 (2011) 540.

[18] C. Kittel, "Physical Theory of Ferromagnetic Domains", Rev.Mod. Phys., 21 (1949) 4.

[19] R.H. Kodama, A.E. Berkowitz, E.J. McNiff, and S. Foner, Phys.Rev.Let., 77 (1996) 394.

[20] H. Mamiya, I. Nakatani, and T. Furubayashi, Phys.Rev.Lett., 80 (1998) 177.

[21] Z.X. Tang, C.M. Sorensen, K.J. Kalabunde, and G.C. Hadjipanayis, Phys.Rev.Lett., 67 (1991) 3602.

[22] V.I. Nikolaev and A.M. Shipilin, "The Influence of Breaking of Exchange Bonds on the Curie Temperature", Physics of the Solid State, 45 (2003) 1079.

[23] W.H. Zhong, C.Q. Sun, and S. Li, "Size Effect on the Magnetism of Nanocrystalline Ni Films at Ambient Temperature", Solid State Commun., 130 (2004) 603.

[24] W.H. Zhong, C.Q. Sun, H.L. Bai, and E.Y. Jiang, "Impact of Bond-Order Loss on Surface and Nanosolid Magnetism" Acta Mater., 53 (2005) 3207.

[25] H.M. Lu, W.T. Zheng, and Q. Jiang, "Saturation Magnetization of Ferromagnetic and Ferrimagnetic Nanocrystals at Room Temperature" J.Phys.D:Appl.Phys., 40 (2007) 320.

[26] W. Gong, H. Li, Z.R. Zhao, and J.C. Chen, J.Appl.Phys., 69 (1991) 5119.

[27] S. Bedanta, "Supermagnetism in Magnetic Nanoparticle Systems", PhD Thesis, 2006.

[28] F. Bodker, S. Morup, and S. Linderoth, "Surface Effects in Metallic Iron Nanoparticles", Phys.Rev.Lett., 72 (1994) 282.

[29] J. Avice, “Surface Effects in AC Heating Process of Magnetic Nanoparticles used in Hyperthermia”, 2013.

[30] C. Q. Sun, W. H. Zhong, S. Li, B. K. Tay, H. L. Bai and E. Y. Jiang, “Coordination Imperfection Suppressed Phase Stability of Ferromagnetic, Ferroelectric and Superconductive Nanosolids”, J. Phys. Chem., 108 (2004) 1080.

[31] W.J. Minkowycz, E.M. Sparrow, and J.P. Abraham, “Nanoparticle Heat Transfer and Fluid Flow”, CRS Press, Baca Raton, London, New York, 2013.

[32] R. Hergt, S. Dutz, R. Muller, and M. Zeisberger, “Magnetic Field Hyperthermia: Nanoparticle Magnetism and Materials Development for Cancer Therapy”, Journal of Physics: Condensed Matter, 18 (2006) 2919.

[33] M. Mahdevi, M.B. Ahmad, Md.J. Haron, and M.Z.A. Rahman, “Synthesis, Surface Modification and Characterisation of Biocompatible Magnetic Iron Oxide Nanoparticles for Biomedical Applications”, Molecules 18 (2013) 7533.

[34] A. Marinin, “Synthesis and Characterization of Superparamagnetic Iron Oxide Nanoparticles Coated with Silica”, Master Thesis, Stockholm, 2012.

[35] P. Abdulkin, T. Houlding, B.R. Knappett, A.B. Lukawska, V. Degirmenci, D.A. Jefferson, G. Kozlowski, E.V. Rebrov, and A.E.H. Wheatley, “Synthesis and Size Control in Magnetically Active Fe and Co Nanoparticle Systems”, in preparation.

[36] S. Zhu, “Synthesis of Size, Structure and Shape Controlled Iron Based Magnetic Nanomaterials”, Master Thesis, Case Western Reserve University, 2012.

[37] G. Kozlowski, Z. Jagoo, A. Lukawska, A. Wheately, Z. Turgut, and H. Kosai, “Ac Magnetic Heating of Superparamagnetic Fe and Co Nanoparticles”, Core Scholar, Wright State University, 2012. Carbon and Oxide Based Nanostructured Materials.

[38] S.P. Gubin, “Magnetic Nanoparticles”, WILEY-VCH Verlag GmbH & Co., 2009.

[39] http://www.fiso.com/admin/useruploads/files/fot-l.pdf (online link).

[40] Z. Jagoo, “Radio Frequency Heating of Magnetic Nanoparticles”, Master Thesis, Ohio Link 2012.

[41] P. MacCabee, V. Amassian, L. Eberle, and R. Cracco, “Magnetic Coil Stimulation of Straight and Bent Amphibian and Mammalian Peripheral Nerve in Vitro: Locus of Excitation”,The Journal of Physiology, 460 (1993) 201.

[42] J.R. LaCourse, W.T. Miller, and M. Vogt, “Effect of High Frequency-Current on Nerve and Muscle Tissue”, Biomed. Eng., IEEE Transactions, 32 (1985) 82.

[43] J. Reilly, “Peripheral Nerve Simulation by Induced Electric Currents: Exposure to Time-Varying Magnetic Fields”, Medical and Biological Engineering and Computing, 27 (1989) 101.

[44] R. Bickford, M. Guidi, P. Fortesque, and M. Swenson, “Magnetic Simulation of Human Peripheral Nerve and Brain: Response Enhancement by Combined Magnetoelectrical Technique”, Neurosurgery, 20 (1987) 110.

[45] http://hyperphysics.phy-astr.gsu.edu/hbase/magnetic/solenoid.html (online link).

[46] http://en.wikipedia.org/wiki/Solenoid (online link).

[47] http://scienceisbeauty.tumblr.com/post/72874066370/tons-of-scientific-imagery-in-here-by-paul (online link for 3-D image of a solenoid).

[48] https://bkpmedia.s3.amazonaws.com/downloads/manuals/en-us/4011A_manual.pdf (online Link for Function Generator).

[49] http://www.mediahex.com/Vacuum_Pump (online link vacuum pump).

[50] E. Cheraghipour, S. Javadpour, and A.R. Mehdizadeh, “Citrate Capped Superparamagnetic Iron Oxide Nanoparticles Used for Hyperthermia Therapy”, Biomedical Science and Engineering, 5 (2012) 715.

[51] J. Motoyama, T. Hakata, R. Kato, N. Yamashita, T. Morino, T. Kobayashi, and H. Honda, "Size Dependent Heat Generation of Magnetic Nanoparticles under AC Magnetic Field for Cancer Therapy", Bio Magnetic Research and Technology, 4 (2008) 6.

[52] W. Andra, C.G. d'Ambly, R. Hergt, I. Hilger, and W.A. Kaiser, "Temperature Distribution as a Function of Time around a Small Spherical Heat Source of Local Magnetic Hyperthermia", Journal of Magnetism and Magnetic Materials, 194 (1999) 197.

[53] P. Pradhan, J. Giri, G. Samanta, H.D. Sharma, K.P. Mishra, J. Bellare, R. Banerjee, and D. Bahadur, "Comparative Evaluation of Heating Ability and Biocompatibility of Different Ferrite-Based Magnetic Fluids for Hyperthermia Application", WILEY Inter Science, (www.interscience.wiley.com), 2006.

[54] M. Matusiewicz, private communication.

[55] H. Khurshid, M. Phan, P. Mukherjee, and H. Srikanth, "Tuning Exchange Bias in Fe/γ- $Fe_2O_3$ Core-Shell Nanoparticles: Impacts of Interface and Surface Spins", Applied Physics Letters, 104 (2014) 072407.

[56] A. F. Rodriguez, A. Kleibert, J. Bansmann, A. Voitkans, L. J. Heyderman, and F. Nolting, "Size-Dependent Spin Structures in Iron Nanoparticles", Physics Review Letters, 104 (2010) 127201.

[57] A. Kakay and L. K. Varga, "Monodomain Critical Radius for Soft-Magnetic Fine Particles", Journal of Applied Physics, 97 (2005) 083901.

[58] K. M. Krishna, "Biomedical Nanaomagnetics: A Spin through Possibilities in Imaging, Diagnostics, and Therapy", IEEE Transactions on Magnetics, 46 (2010) 2523.

[59] R. E. Rosensweig, "Heating Magnetic Fluid with Alternating Magnetic Field", Journal of Magnetism and Magnetic Materials, 252 (2002) 370.

[60] M. A. Verges, R. Costa, A. G. Roca, J. F. Marco, G. F. Goya, M. P. Morales, and C. J. Serna, "Uniform and Water Soluble Magnetic Nanoparticles with Diameters Around the Monodomain-Multidomain Limit", Journal of Applied Physics, 41 (2008) 134003.

[61] http://en.wikipedia.org/wiki/Gas_constant.